Numerical Study on the Occurrence and Sensitivity of a High-Frequency Instability in an Advanced Can-Annular Combustion System

by

M. Zaky

to obtain the degree of Master of Science
at the Delft University of Technology,
to be defended publicly on Friday May 21st, 2021 at 01:00 PM.

Student number:	4459318	
Project duration:	February 3, 2020 – December 18, 2020	
Thesis committee:	Prof. dr. ir. S. Klein,	TU Delft, supervisor
	Prof. dr. ir. D. Roekaerts,	TU Delft
	Dr. ir. L. Panek,	Siemens Energy, supervisor

This thesis is confidential and cannot be made public until May 21, 2023.

TU Delft SIEMENS energy

Acknowledgements

Hereby I would like to express my sincere gratitude to all who have contributed in making this study possible, and without whom I would not have been able to complete this project.

First I would like to thank my supervisor Prof. Sikke Klein for bringing me in contact with Siemens Energy and for his continued involvement throughout despite the long distance. Thank you for the invaluable guidance and constructive feedback throughout the project.

Secondly I would like to thank my daily supervisor Dr. Lukasz Panek. The brainstorming sessions we had and the patience you had while explaining new topics to me helped me write a thesis I'm proud to present. In addition to the academic advice you also provided me with excellent restaurant and activity recommendations, making my stay in Berlin even more enjoyable.

Next I would like to express my gratitude to Dr. Bernhard Wegner for allowing me to write my thesis at Siemens. Not only did you enable me to continue working during the pandemic, you also ensured I had all the options and resources to do this.

I want to thank Tim and Svetoslav, two fellow students and friends who I spent countless hours in and outside the office with. The stay abroad would have been a lot less fun without you there.

Thank you Mees, Meghan, Rama, Marko, Lim and Stefan for constantly checking up on me during my time abroad and this pandemic. I never felt like I was out there on my own.

To my parents, Atef and Nahed for their unconditional love and support. For making sure I had everything I needed so that I can study without worrying about anything else. To my sister Karen, for being there to remind me that everything works out in the end, however difficult things may seem in the moment.

And last, but certainly not least, I want to thank Melody. You were always there to cheer me on and motivate me whenever I needed it and you made this journey a lot more enjoyable.

Abstract

Gas turbines for power generation use lean premixed flames to adhere to the strict pollutant emissions regulations. Unfortunately, this often leads to thermoacoustic instabilities. These instabilities can lead to failure of system components, flame blow-off or flashback and a reduction in efficiency. Especially the high frequency transverse thermoacoustic instabilities can lead to big problems in the successful operation of gas turbines. These instabilities can be reduced by adding damping devices or mitigating the excitation mechanisms. In this work, Large Eddy Simulation (LES) is used to identify the thermoacoustic instability which tends to occur in a specific heavy duty gas turbine combustor design. In order to successfully counteract this instability, identification of the acoustic mode affecting the burner is required. Results from the LES are compared with experiments to test the predictability of LES and research mitigation techniques. The oscillation amplitudes do not match due to numerical damping, but the frequency of the oscillation in LES is within 1% of the experimental value. Furthermore, a coherence between the heat release and pressure oscillations of 80% is achieved and the phase of the oscillations are within 90° of each other. This confirms that the Rayleigh criteria is satisfied and the instability in the simulation is indeed a self-excited thermoacoustic instability. After identifying the mode, Fast Fourier Transform (FFT) of the pressure data at the combustor walls is used to visualize and locate the mode. Its location suggests that fuel supply oscillations could be a possible driving mechanism. However, the frequency of the oscillations in the fuel supply did not match that of the thermoacoustic instability so this hypothesis was rejected. After identifying the mode, the effect of different simulation and operation parameters is researched. First a model coefficient which influences the flame length is changed. Shortening the flame results in a higher amplitude instability, due to the location of maximum heat release moving closer to the location of the source of the instability. Next, the fuel distribution is changed in order to break flame symmetry and reduce the instability amplitude. This is done successfully, as the amplitude of the instability at the peak frequency is reduced to the same level as the surrounding noise frequencies. Finally, the effect of adding Helmholtz resonators specifically designed for the instability of interest is researched. A transfer function is defined to measure the response of the resonators to a pressure fluctuation in front of them. The result is compared to an analytical solution to determine the effectiveness of the resonators. Like the fuel biasing, also the resonators performed well and resulted in a decrease of the instability amplitude.

Keywords: *CFD, LES, Gas Turbines, Combustion Instability, Thermoacoustics, Lean Premixed Combustion, Fuel Staging, Helmholtz Resonators*

Contents

List of Figures

List of Tables

1 Introduction

1.1 Motivation

Gas turbines are an efficient alternative to coal power generation. With their fast start up times and fuel flexibility, they are well suited to support renewable power generation and modern dynamic grids. These are aspects making them very attractive for future applications.

Gas turbines for power generation and propulsion have traditionally been using diffusion-flame combustors because of their reliability. A downside of these types of combustors is that they generally produce high amounts of NO_x. The increasingly strict regulation for pollutant emissions has led engine manufacturers to develop combustors that meet various regulatory requirements [1]. The main emissions abatement strategy, lean premixed combustion, has lead to a rise in the severity and the more frequent appearance of instabilities in these engines [2]. Thermoacoustic instabilities arise naturally and are self- sustained. It is a phenomenon whereby acoustic pressure and heat release rate fluctuations interact. Under certain conditions the acoustic oscillations lead to fluctuations in the heat release rate that in turn feed energy back to the acoustic field [3]. The occurrence of these instabilities is undesired, since it can lead to low- or high-cycle fatigue of system components, and flame blow-off or flashback. This in turn could lead to expensive downtime for repair or maintenance [4].

1.2 Problem description

One of the most important reasons why gas turbine combustor flames are prone to thermoacoustic instabilities is the combination of two fundamental causes [5]. Firstly, the amount of energy needed to generate large amplitude oscillations is negligibly small compared to the amount of energy available due to the combustion process. Generally, less than 0.1% of the energy released in the chemical process is enough to induce pressure fluctuations with an amplitude equal to that of the mean pressure in the combustion chamber [1]. Secondly, combustion chambers are relatively acoustically closed, meaning that there is not much possibility of acoustic damping. In addition, the acoustic waves can propagate throughout the entire combustion chamber and affect the flame dynamics because of this [1]. Therefore, a prerequisite of any instability research is the identification of the acoustic modes in the combustion chamber.

Siemens has done experiments at DLR in Cologne with the 8000H combustor. This burner is used in the 8000H heavy duty gas turbine, illustrated in figure 1.1. A high frequency acoustic mode was found. This mode will be further investigated in this thesis with means of computational fluid dynamics. The focus of the thesis will be on a combustor design, in which reproducible high frequency dynamics can be observed. Although mitigation strategies for stable operation exist, a deeper understanding of the instability cause is desirable in order to successfully counteract this instability. Such instabilities can be

reduced by adding acoustic damping or the mitigation of the excitation mechanisms. For this purpose a literature study is conducted before analyzing the instability in the 8000H combustor.

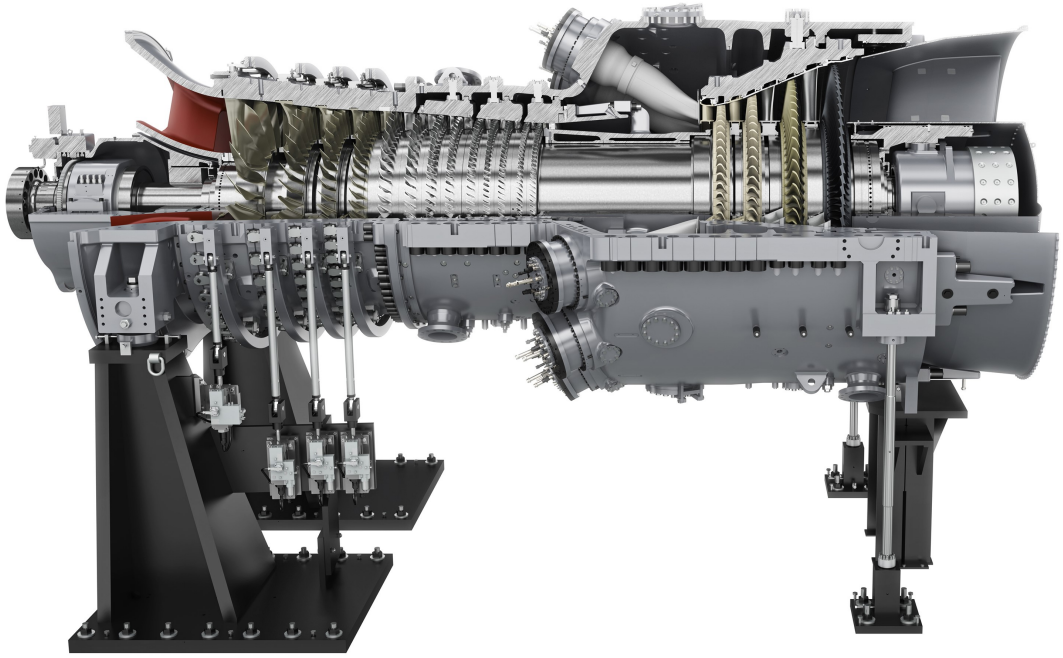

Figure 1.1: Siemens SGT6-8000H heavy-duty gas turbine. Can-type 8000H combustor visible near top-part of this image. Courtesy of Siemens-Energy [6].

1.3 Project scope and objective

In order to gain a deeper understanding of the instability cause and to get a step closer to completely avoiding the mode, the following research questions will be answered:

- Can the mode found in the experiments at DLR be reproduced using Large Eddy Simulations?
  - How does the frequency of the mode in LES compare with the frequency in experiments?
  - What does the mode look like and where is it located inside the burner?
- How do different operational parameters influence the presence and characteristics of the mode?
- How well do the resonators on the burner perform and how do they influence the mode?

2 Literature study

Since thermoacoustic instabilities occur from the coupling between heat release fluctuations and acoustics, the basics of both combustion and acoustic theory are covered in sections 2.1 and 2.2 respectively. Afterwards, combustion instabilities and relevant terms will be explained in section 2.3. Next, examples of driving mechanisms for thermoacoustic instabilities in a gas turbine will be discussed in section 2.4 and mitigation techniques relevant for this work will be given in section 2.5. Finally, the relevant information about the simulation technique to be used will be given in section 2.6.

2.1 Flow and Combustion Theory

First the governing equations of reacting flow will be given. Afterwards the basics of turbulence will be discussed and finally the different combustion types relevant for gas turbine flames will be discussed.

2.1.1 Governing equations

To fully describe the reacting flow in the burner, a set of equations has to be solved. In addition to the continuity equation (1), momentum equation (2) and energy equation (4), conservation equations need to be solved for the species mass fractions Y_i involved in the combustion process. This is done for species $k = 1$ to N in equation (3).

$$\frac{\partial \rho}{\partial t} + \frac{\partial \rho u_i}{\partial x_i} = 0 \tag{1}$$

$$\frac{\partial}{\partial t}\rho u_j + \frac{\partial}{\partial x_j}(\rho u_i u_j) = -\frac{\partial p}{\partial x_i} + \frac{\partial \tau_{ij}}{\partial x_j} \tag{2}$$

$$\frac{\partial \rho Y_k}{\partial t} + \frac{\partial}{\partial x_i}\left(\rho\left(u_i + V_{k,i}\right) Y_k\right) = \dot{\omega}_k \tag{3}$$

$$\frac{\partial \rho h}{\partial t} + \frac{\partial}{\partial x_i}\left(\rho u_i h\right) = \frac{Dp}{Dt} - \frac{\partial q_i}{\partial x_i} + \tau_{ij}\frac{\partial u_i}{\partial x_j} + \rho \sum_{k=1}^{N} Y_k f_{k,i} V_{k,i} + \dot{\omega}_t \tag{4}$$

2.1.2 Turbulence

Turbulence is an important part of fluid mechanics and is found in almost all real life engineering applications, as well as in nature. It plays an important part in transport phenomena like heat transfer, mass transfer and flow-induced mixing. It therefore has large effects on combustion since reaction rates are strongly dependent on the mixing of fuel and oxidizer [7]. Because of its large influence on combustion, some basic properties of turbulent flows will be briefly touched upon before discussing combustion.

Reynolds number The most common dimensionless number in fluid mechanics is the Reynolds number as defined in equation (5). It relates the destabilizing inertial forces to the stabilizing/damping viscous forces of a flow [8]. The Reynolds number indicates whether a flow is laminar or turbulent. Laminar flows are smooth, ordered and have a regular/layered structure. The viscous forces are dominant in these flows, resulting in a small Reynolds number. Turbulent flows on the other hand are disordered, chaotic and fluctuating. Inertial forces dominate these types of flows and thus have large Reynolds numbers.

$$Re = \frac{\rho U L}{\mu} \tag{5}$$

Figure 2.1 illustrates the effect turbulence has on a flame. In the left picture, a smooth laminar flame is visible with a Reynolds number around 400. The Reynolds number increases up to 4000 in the rightmost picture and displays a chaotic structure with chaotic motions [7].

Figure 2.1: Transition from laminar (left) to turbulent flames (right). Reynolds number increases from 400 to 4000. Obtained from the work of Nieuwstadt et al. [7]

Energy Cascade Turbulence exists in vortex-like structures with varying dimensions called eddies. The turbulent structure with the largest eddies is referred to as the macrostructure. The macrostructure is associated with a length scale $\mathcal{L}$ and velocity scale $\mathcal{U}$. These scales are proportional to the size and geometry of the flow. Furthermore, from experience it is know that turbulence is strongly dissipative and diffusive. The large eddies break down into smaller eddies, thus transferring their energy to the smaller scales. This process continues until the eddies become so small that viscous effects cannot be neglected anymore and energy is dissipated through viscosity in the form of heat. This happens at the microstructure. This process is called the Energy Cascade [7]. The energy cascade process forms the basis of many turbulence closure models [9]. The rate at which energy from the macrostructure is dissipated through viscous dissipation at the microstructure is given by equation (6):

$$\epsilon \propto \frac{\mathcal{U}^3}{\mathcal{L}} \tag{6}$$

Similar to the macrostructure, also the microstructure has characteristic scaling parameters, known as the Kolmogorov scales. Based on the assumption that only the viscosity ν and dissipation rate of kinetic energy ϵ are important at this level of turbulence, the Kolmogorov length, time and velocity scales can be defined as:

$$\eta = \left(\frac{\nu^3}{\epsilon}\right)^{\frac{1}{4}}, \quad \tau = \left(\frac{\nu}{\epsilon}\right)^{\frac{1}{2}}, \quad v = (\nu\epsilon)^{\frac{1}{4}} \tag{7}$$

It follows from (7) that the Reynolds number at the microstructure $Re = \frac{v\eta}{\nu}$ equals unity, further confirming that the microstructure is dominated by viscosity. The Kolmogorov scales will be used in other dimensionless numbers for combustion classification in a later section.

2.1.3 Combustion Types

Now that basic notions of fluid mechanics have been given, combustion will be discussed. Processes in combustion can be subdivided in terms of mixing (premixed, partially premixed and non-premixed), in terms of chemical timescales (fast and slow chemistry) and whether the flow is laminar or turbulent. For non-premixed combustion, the oxidizer and fuel meet at the flame front. Non-premixed flames are also called diffusion flames. Slow chemistry is not often found in practical applications, as this means that the combustion happens at a temperate close to the extinction temperature, for example low-NOx burners. Typically lean-burn gas turbine combustion happens under premixed conditions with turbulent flames [9].

Laminar combustion will be briefly discussed as this forms a stepping stone to turbulent combustion. Afterwards the focus will be on premixed turbulent combustion.

Laminar Premixed Combustion For laminar premixed flames, the fuel and oxidizer are mixed before entering the reaction zone and the flow is laminar. Examples of laminar premixed flames are 1D planar flames in a duct or and conical shaped flames in a (lean burning) Bunsen burner, as seen in figure 2.2 [10].

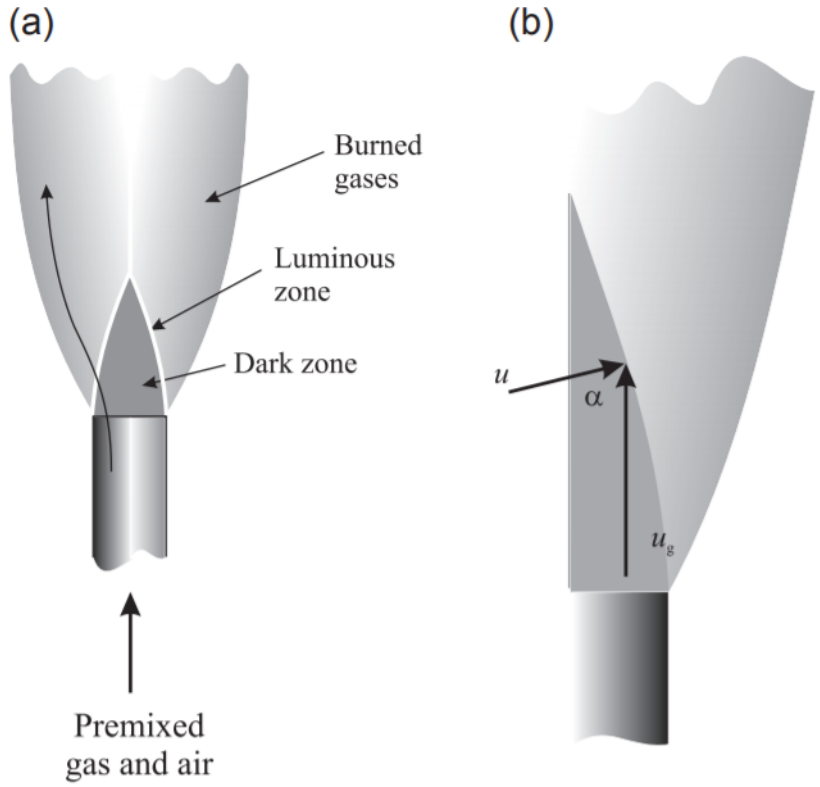

Figure 2.2: Schematic diagram of Bunsen burner flame in a general arrangement (a) and with velocity vectors (b). Obtained from the work of Winterbone and Turan [11].

In laminar premixed combustion, the heat released by reaction preheats the reactants by diffusion until reaction starts in the newly provided fresh mixture. The flame front or reaction zone can be seen as a propagating into the unburnt mixture and is displayed as the *luminous zone* in figure 2.2. This propagation into the fresh mixture happens with the most relevant quantity in laminar premixed combustion known as the laminar flame speed. The laminar flame speed u in premixed combustion only depends on the fuel-to-air equivalence ratio ϕ, the temperature of the unburnt mixture T_u and the pressure p [11].

Even though most practical flames are turbulent, the laminar flame speed is usually a good indication of the flame velocity under other circumstances [11]. To determine the laminar burning velocity S_L in a Bunsen burner as in figure 2.2(b), the angle α and the flow velocity of the unburnt mixture u_g through the relation:

$$S_L = u_g sin(\alpha) \tag{8}$$

Turbulent premixed combustion In turbulent combustion, the flame front is not flat anymore due to the eddies present in the flow. The eddies interact with the flame front and it becomes wrinkled. Combustion requires fuel and oxidizer to mix at a molecular level and turbulence enhances this mixing. During the breakdown of eddies, strain and shear will increase, leading to steeper concentration gradients at the interface between

reactants which in turn enhances the molecular inter-diffusion. So the molecular mixing takes place at the interface of the small eddies [9].

Turbulent premixed combustion is typically described through the use of the Borghi diagram. This diagram shows different combustion regimes as a function of the ratio turbulent velocity fluctuation to laminar flame speed u'/S_L and the ratio of the integral length scale to the laminar flame thickness l_t/l_L, plotted on a log-scale. The different regimes with different flame behavior are divided by lines corresponding to dimensionless numbers equal to unity. The dimensionless numbers are the turbulent Reynolds number Re_T, the Karlovitz number Ka and the Damköhler number Da.

$$Re_T = \frac{u' l_t}{\nu}, \qquad Ka = \frac{t_L}{\tau}, \qquad Da = \frac{t_t}{t_L} = \frac{l_t S_L}{u' l_L} \tag{9}$$

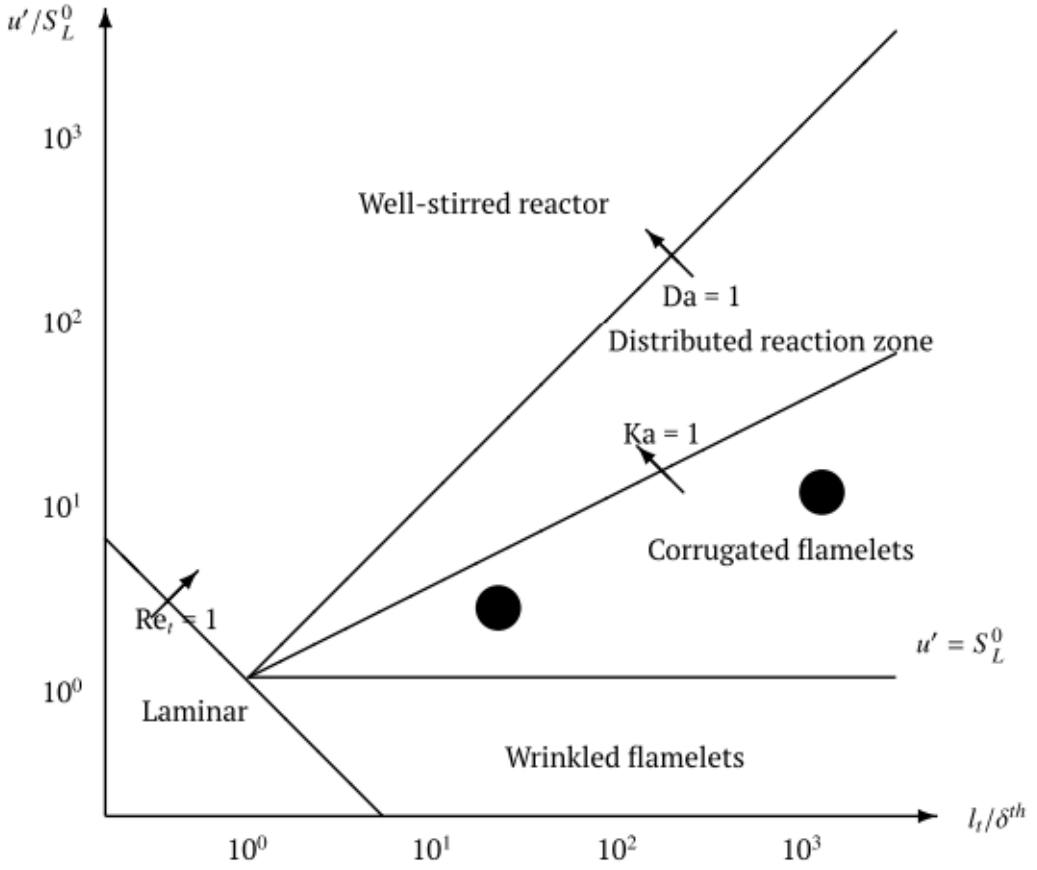

Figure 2.3: Borghi diagram. The left dot indicates the premixed combustion regime typical for laboratory-scale studies. The right dot indicates the combustion regime typical at take-off of current gas turbine engines. Obtained from the work of Palies [12].

When Re_T is smaller than unity, laminar plane flame fronts are observed. The domain for turbulent flames ($Re_T > 1$) is then further divided in three regions.

The Karlovitz number is the ratio between the timescale $t_L = l_L/S_L$ of a laminar flame and the Kolmogorov timescale τ. When Ka is smaller than unity, the chemical timescale of the flame is shorter than the turbulence timescale and the eddies don't have enough time to enter the flame front. The flame front thickness is smaller than the turbulent scales resulting in the flame front becoming wrinkled. This region is further divided in corrugated flames with pockets of burnt and unburnt gas and the laminar wrinkled flame fronts, depending on the turbulence intensity [12].

The Damköhler number is the ratio between the integral turbulent timescale or the timescale associated with the macrostructure t_t and the timescale of the laminar flame chemistry t_L. When the Damköhler number is smaller than unity, the time needed for chemical change is smaller than the time needed for change induced by turbulence. Therefore nearly all of the turbulent eddies are embedded in the flame and no clear flame front can be defined [10]. This region is called the ideally stirred reactor.

The last region defined is the distributed reaction zone or thickened flame regime. This region corresponds to a Damköhler and Karlovitz number larger than unity. Here a small part of the eddies is embedded in the flame front.

Depending on the type of turbulent combustion, different turbulent flame speed relations have been developed. This will further be discussed in section 2.6.3.

2.2 Acoustics

Acoustics can be seen as the study of small pressure perturbations propagating as a wave in a compressible fluid. These velocity and pressure fluctuations can be described using the acoustic wave equation which is derived from the conservation of mass (1), momentum (2) and energy equations (4) [13].
The general form of the wave equation or wave equation in a reacting flow as formulated in Poinsot [14] is given by equation (10).

$$\boldsymbol{\nabla} \cdot \left(c_0^2 \boldsymbol{\nabla} p'\right) - \frac{\partial^2}{\partial t^2} p' = -\left(\gamma - 1\right) \frac{\partial \dot{\omega}_T}{\partial t} - \gamma p_0 \boldsymbol{\nabla} \vec{u} : \vec{u} \tag{10}$$

Here p' is the acoustic pressure fluctuation p_0 and c_0 the mean pressure and mean speed of sound respectively, $\dot{\omega}_T$ the heat release, $\gamma = C_p/C_v$ the specific heat ratio. The turbulent flow noise term $\boldsymbol{\nabla}\vec{u} : \vec{u}$ term is usually neglected due to it being small compared to the acoustic source term related to heat release.

2.2.1 One-dimensional planar waves

To gain a better understanding of the wave equation, the solution for a planar wave in a one-dimensional duct with non-reacting flow will be given and discussed. The wave equation for non-reacting flow takes on the simpler form:

$$\boldsymbol{\nabla}^2 p' - \frac{1}{c_0^2} \frac{\partial^2 p'}{\partial t^2} = 0 \tag{11}$$

To solve this equations for a one-dimensional planar wave, the assumption can be made that the wave is a superimposition of two waves traveling in opposite direction [13]. The solution for the pressure fluctuation is then given as in equation (12). If this equation is then inserted in the linearized momentum equation, also the solution for the velocity fluctuation is obtained as in equation (13):

$$p' = f(x - c_0 t) + g(x + c_0 t) \tag{12}$$

$$u' = \frac{1}{\rho_0 c_0} \left(f(x - c_0 t) + g(x + c_0 t)\right) \tag{13}$$

Here f and g denote the waves traveling in positive and negative directions respectively and ρ_0 the density of the fluid.

Harmonic solution The wave equation is usually solved in the frequency domain. This is done by assuming that the pressure fluctuations are of harmonic nature and fluctuate at a frequency of $f = \frac{\omega}{2\pi}$. The harmonic pressure is written in complex notation as $p'(x,t) = \hat{p}(x)e^{i\omega t}$, where $\hat{p}(x)$ is the amplitude and ω the angular frequency of the oscillation. When this notation is used in the wave equation (11), the Helmholtz equation is obtained:

$$\boldsymbol{\nabla}^2\hat{p} + k^2\hat{p} = 0 \tag{14}$$

Here $k = \frac{\omega}{c_0}$ denotes the wave number. The solution for the pressure and velocity fluctuations in Eq. (12) and Eq. (13) are then obtained from Eq. (14) in a similar way:

$$\hat{p} = \hat{f}e^{i(\omega t - kx)} + \hat{g}e^{i(\omega t + kx)} \tag{15}$$

$$\hat{u} = \frac{1}{\rho_0 c_0}\left(\hat{f}e^{i(\omega t - kx)} + \hat{g}e^{i(\omega t + kx)}\right) \tag{16}$$

When only the positive traveling wave is considered, the relation between the pressure and velocity fluctuation is such that $p' = \rho_0 c_0 u'$. This scaling factor $\rho_0 c_0$ is called the characteristic impedance of the fluid through which the wave propagates [15]. It can be seen as the resistance the fluid has against motion due to the acoustic pressure fluctuation. Impedance will be further discussed in the next section.

2.2.2 Impedance and Reflection

Two useful quantities in acoustics are the impedance Z and reflection coefficient R. The impedance of a boundary or any arbitrary section can be defined as:

$$Z(\omega) = \frac{1}{\rho_0 c_0}\frac{p'}{u'} = R_a + i\chi \tag{17}$$

The impedance is a complex number and depends on ω. The real part of the impedance is called the resistance R_a and the imaginary part the reactance χ. These terms will be further explained in section 2.5.2.

The reflection coefficient is defined as the ratio between the amplitude an outgoing wave which is reflected by an impedance Z to the amplitude of an incoming wave at a selected surface [16]. It can be written as a function of the impedance by inserting equations (15) and (16) in (17) and rewriting:

$$R(\omega) = \frac{\hat{g}(\omega)}{\hat{f}(\omega)} = \frac{Z(\omega) - 1}{Z(\omega) + 1} \tag{18}$$

Acoustic boundary conditions To further clarify impedance and reflection, a few examples will be briefly discussed now. The first example is that of an infinitely long duct towards $x = +\infty$ with a wave traveling in the positive x-direction. The wave will never be reflected and thus only a wave traveling in the positive direction will exist. This results in $R = 0$ and $Z = 1$.

The next example is that of a duct terminating in a larger section as seen in figure 2.4. The pressure at the boundary imposes no pressure fluctuations to occur, giving an impedance of $Z = 0$ and reflection coefficient of $R = -1$. This means the incoming wave will be reflected but with a phase shift of 180°, canceling out the perturbation.

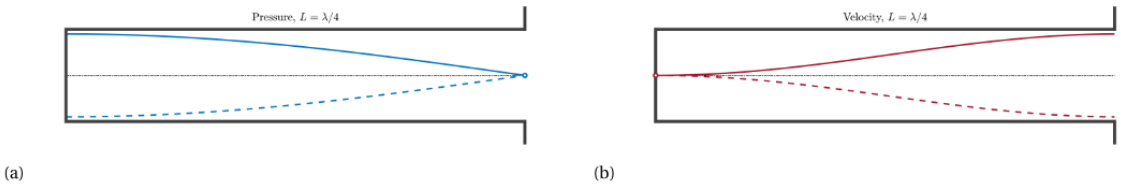

Figure 2.4: Schematic of a duct terminating in an open section. The pressure (a) and velocity (b) distribution are shown for their peak values in their periods. Obtained from the work of T. Dammers [17].

The last example is that of a duct closed of at both ends as seen in figure 2.5. Since the the velocity at a wall goes to zero, the impedance will tend to infinity and the reflection coefficient becomes unity. The incoming waves will be fully reflected.

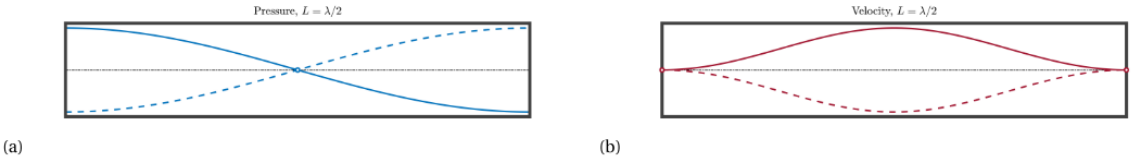

Figure 2.5: Schematic of a duct with two closed ends. The pressure (a) and velocity (b) distribution are shown for their peak values in their periods. Obtained from the work of T. Dammers [17].

2.2.3 Acoustic Resonance

Acoustic resonance can be explained with the previously given scenario of a traveling wave inside a closed duct as in figure 2.5. When the frequency of the harmonic wave matches that of the natural frequency of the duct, the system starts to resonate and the wave will get amplified. A system can have multiple resonance frequencies, called harmonics. For the mentioned duct, the resonant frequencies can be given by:

$$f = \frac{nc_0}{2L} \tag{19}$$

where c_0 and L are the speed of sound of the fluid in the duct and the length of the duct. Every solution to this equation is called a mode with the integer n being the mode order. When looking at the pressure distribution in figure 2.5(a), non-zero amplitudes, also called anti-nodes are seen at the walls and zero amplitudes, also called node, is seen in the middle.

2.2.4 3D Helmholtz equation

So far only one dimensional waves have been discussed. Since the focus of this work will be on a gas turbine combustor, the extension to 3D acoustics needs to be made. The 3D wave equation (10) given at the beginning of this section is also solved by assuming harmonic fluctuations. This time not only for pressure, but also for the heat release term $\dot{\omega}$, where $\hat{\Omega}_T$ is the amplitude:

$$p' = \hat{p}\,(x, y, z)\, e^{-i\omega t} \quad \text{and} \quad \dot{\omega}_T = \hat{\Omega}_T e^{-i\omega t} \tag{20}$$

When (20) are inserted in (10), the Helmholtz equation becomes:

$$\boldsymbol{\nabla} \cdot \left(c_0^2 \boldsymbol{\nabla} \hat{p}\right) + \omega^2 \hat{p} = i\omega\,(\gamma - 1)\,\hat{\Omega}_T \tag{21}$$

This equation is the basis of three-dimensional Helmholtz codes, which will be discussed in section 2.2.5 after discussing the 3D mode shapes.

Mode shapes The 8000H combustor is a can-type combustor. This means that it can be compared to a three-dimensional cylindrical shaped duct. The equation to determine the resonant modes becomes (22). For a hard-walled cylinder with length L and radius r, the resonant frequencies in axial (n), radial (m) and tangential/azimuthal (j) directions are calculated by solving equation (22). In this equation, β stands for the eigenvalue of the Bessel function [18]:

$$f_{nmj} = \frac{c_0}{2\pi} \sqrt{\left(\frac{n\pi}{L}\right)^2 + \left(\frac{\beta_{mj}}{r}\right)^2} \tag{22}$$

The different solutions or modes are given in figure 2.6:

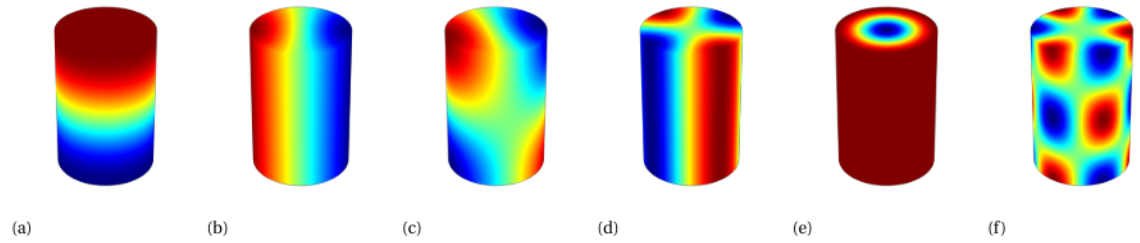

Figure 2.6: Examples of mode shapes in an arbitrary chosen hard-walled cylinder, from left to right are depicted: a) first longitudinal mode (1L), b) first transverse mode (1T), c) combined first longitudinal and transverse mode (1T1L), d) second transverse mode (2T), e) first radial mode (1R), f) combined second longitudinal and third transverse mode. Red shows zones of positive pressure amplitude and blue negative amplitude. Obtained from the work of T. Dammers [17].

Standing and turning modes Similarly to the forward and backward traveling waves in a 1D-duct, the transverse modes displayed in figure 2.6 can be viewed as a combination of waves propagating in azimuthal direction [19]. To first order, it can be described by a combination of two simple one-dimensional waves propagating in opposite direction along the azimuthal direction θ [14]. The waves can be expressed as in equation (23):

$$p' = \hat{f} e^{i(\theta - \omega t)} + \hat{g} e^{i(-\theta - \omega t)} \tag{23}$$

where $\hat{f}$ and $\hat{g}$ are the amplitudes of the clockwise and counterclockwise turning wave respectively. Now three scenarios can be defined: If $\hat{f}$ and $\hat{g}$ are of equal magnitude, the

mode will be standing. If one of the two waves has 0 magnitude the mode will rotate in the direction of the nonzero amplitude. Finally, if $\hat{f}$ and $\hat{g}$ are non-zero and of non-equal amplitude a mixed mode will appear. This mode will have a more complex structure.

2.2.5 Solutions to the Helmholtz equations

There are two approaches to solving the Helmholtz equation (21). The first one is by neglecting the effect of the unsteady heat release perturbation $\hat{\Omega}_T$, thus setting the RHS to zero. Knowing the sound speed c distribution, i.e. knowing the local composition and temperature, it provides the eigenfrequencies ω_k and the associated structure of the mode $p'_k(x, y, z)$ in the burner.

This has shortcomings in the way that it does not take the flame effect as an active acoustic element into account and thus does not take the coupling between the heat release and pressure fluctuations into account. Previous work on the burner has been done using this approach. It lead to roughly 90 different eigenmodes in a 200 Hz frequency range around the frequency of interest. Due to confidentiality reasons, the work cannot be cited. A lot can be learned from an analysis like this, but the actual mode shape that affects the burner in real life remains uncertain. Furthermore the resulting eigenfrequencies and their modeshape can be used to compare with the results from the second approach, which will be discussed below.

The second approach does take the heat release perturbations $\hat{\Omega}_T$ into account. It requires a model to link $\hat{\Omega}_T$ and $\hat{p}$ together. This can be achieved through Large Eddy Simulations, the approach taken in this work. Large Eddy Simulations are discussed in section 2.6.

2.3 Gas turbine combustion instabilities

The term *instability* characterizes a phenomenon where a small perturbation could result in a large response in the system. This response could be so big that the system variables grow to very large amplitudes. In some cases, the system variables could reach large amplitude oscillations and a new system gets established. This is called a limit cycle [20] of which an example is given in figure 2.7.

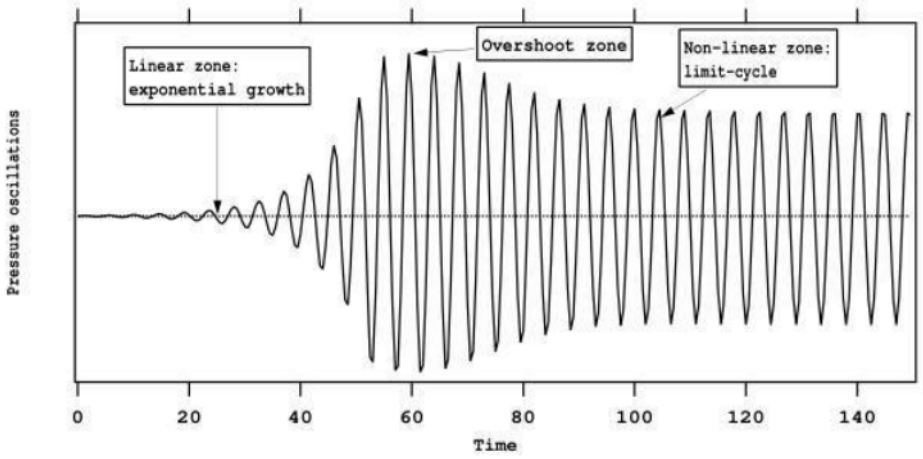

Figure 2.7: Growth of a combustion instability to limit cycle. Obtained from the work of Poinsot & Veynante [14].

Thermoacoustic instabilities arise from interaction of acoustic waves and unsteady heat release [20]. It is a positive feedback cycle that typically involves three steps as displayed in figure 2.8. Heat release fluctuations add energy to the acoustic field. This leads to pressure and velocity fluctuations which in turn lead to fluctuations to the flow field and mixture composition. Because of fluctuations in the fuel/air ratio, the heat release at different locations of the flame will also fluctuate. This closes the feedback loop, as seen in figure 2.8 and combustion instabilities can manifest [21]. They lead to many undesirable effects like [22]:

- large amplitude structural vibrations
- Increased heat flux at the combustor walls
- flashback into the premixer
- flame blow-off

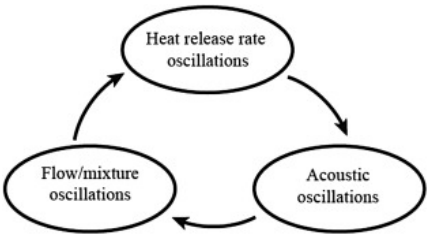

Figure 2.8: Thermoacoustic feedback cycle. Obtained from the work of O'Connor et al. [21].

2.3.1 Rayleigh Criteria

In order for thermoacoustic instabilities to occur, the well-known Rayleigh criteria needs to be satisfied. The Rayleigh criteria states that if the pressure and heat release fluctuations are within a 90° phase with each other, the thermoacoustic instability is fed by the coupling between acoustics and the flame [23]. In the most general form, the Rayleigh criteria is written as (24):

$$\int_T p'(t)q'(t)dtdV > 0 \tag{24}$$

This form of the Rayleigh criteria is only valid for undamped systems. However, real systems also have acoustic damping. It is possible to extend the Rayleigh criteria (25), taking also the acoustic losses into account [24]:

$$\int_T \int_V p'(\mathbf{x},t)q'(\mathbf{x},t)dtdV > L \tag{25}$$

Here L accounts for the acoustic losses of the system. These losses come from different sources like losses at the inflow and outflow boundaries, i.e. when the inlets or outlets are chocked [25], radiation, viscous dissipation [17], Helmholtz resonators which target acoustics at specific frequency ranges [21] or bias flow liners which transfer acoustic energy into vortices [26]. When the pressure and heat release fluctuations are out of phase, they can even damp the acoustic oscillation [25].

2.3.2 Classification of thermoacoustic instabilities

Thermoacoustic instabilities in gas turbines are usually classified by the frequency range at which the oscillations happen. They can be classified as Low (LFD), Intermediate (IFD) and High frequency dynamics (HFD). There is no universally accepted threshold for the different categories. Typically however LFD, also called 'rumble', occurs at frequencies below 100 Hz. IFD occurs between 100-1000 Hz and finally HFD or 'screech' happens above 1000 Hz. [1]. Observing HFD is not as common as LFD or IFD, but it is particularly destructive to engine hardware. Parts of the combustor can fail within minutes of high amplitude of HFD [4]. An example of damage resulting from HFD is shown in figure 2.9. Several welds attaching the burner nozzles to the premixed failed causing the premixed tubes to break. The focus of this work will on HFD.

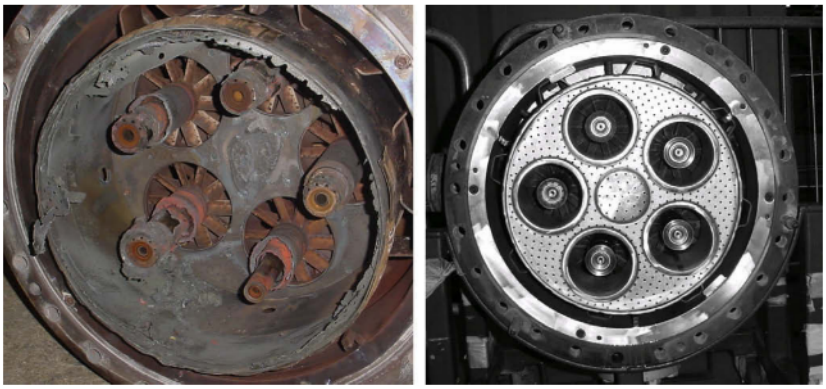

Figure 2.9: Burner assembly damaged by HFD (left) with a new burner assembly (right) as comparison. Obtained from the work of Goy et al. [27].

2.4 Driving Mechanisms

Different processes may contribute to the positive feedback loop mentioned before. These so called driving mechanisms perturb the flow in different ways, but in general these perturbations are coupled back to the driving mechanism through a feedback process. These feedback processes involve time-lags, since the effect of perturbations upstream of the flame need to be convected downstream to the flame front. In general, systems with time-lags tend to be more unstable [22]. Different driving mechanisms have been discussed by T. Lieuwen and V. Yang [4], S. Ducruix et al. [22], Y. Huang [1] and J. O'Connor et al. [21]. A brief summary of some driving mechanisms will be given in the next paragraphs to sketch a general idea about the complexity of the problem at hand.

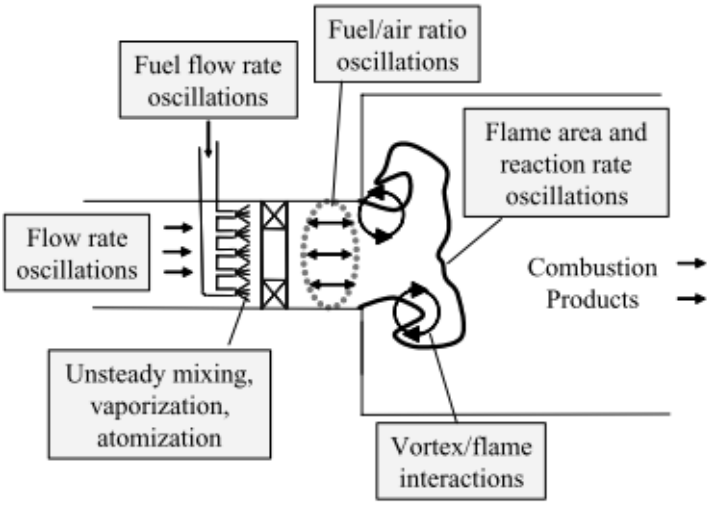

Figure 2.10: Example of different flow and flame processes that can drive combustion instabilities. Obtained from [4].

2.4.1 Equivalence ratio fluctuations

Pressure oscillations that happen at the flame propagate upstream into the premixing sections of the combustor. The mixing of air and fuel gets disturbed and thus the equivalence ratio ϕ will fluctuate. This mixture fluctuation gets convected downstream towards the flame and results in heat release fluctuations [4]. Studies have shown that these fluctuations ϕ' can result in very large heat-release oscillations in lean operating conditions like those in the 8000H combustor [28]. In some cases it can be the primary cause of the heat release fluctuations [29]. Experiments done by Zukoski [30] have shown that the reason why lean combustion is susceptible to this type of driving mechanism is due to the varying chemical timescale. Figure 2.11 shows the relation between the equivalence ratio ϕ and the chemical timescale τ_{chem}. Lean combustion happens at an equivalence ratio below unity. The reaction rate is strongly dependent on the chemical timescale and as can be seen from the large gradient in 2.11, a small change in equivalence ratio can lead to a large change in the reaction rate [1].

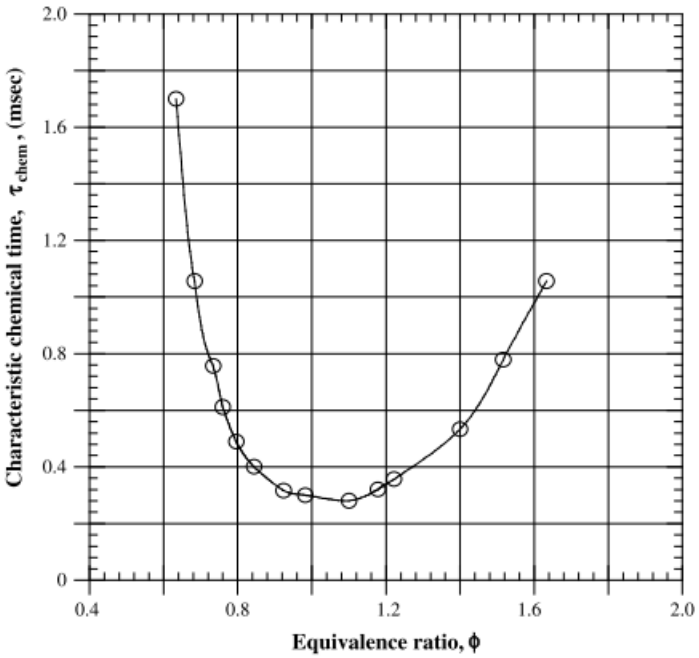

Figure 2.11: Experimentally obtained relation between chemical timescale and equivalence ratio. Obtained from [30].

2.4.2 Flame Surface Variations

Acoustic velocity fluctuations can cause periodic changes of the flame surface area, resulting in heat release fluctuations. These velocity fluctuations can for instance come from the burner exhaust and are convected towards the flame front [22]. The heat release per unit volume for the simple case of a premixed laminar flame can be expressed as:

$$\dot{Q} = q\rho_u S_L A \tag{26}$$

Here A is the flame surface area, S_L the laminar flame speed, ρ_u the density of the unburnt fuel/air mixture and q the heat of reaction per unit mass. Assuming everything remains constant except for the surface area when velocity fluctuations reach the flame surface, the fluctuation in heat release becomes proportional to surface area fluctuation [1]. Because the flow in the burner is highly turbulent, large heat release oscillations can thus occur.

2.4.3 Vortex Shedding

The next driving mechanism is flame-vortex interaction [31]. There are two main pathways for this interaction to generate instabilities. Coherent vortical structures resulting from separation at the flame holder or from vortex breakdown due to the swirl flows (found in gas turbine combustors) can entrain fresh fuel gas mixture. Ignition will take place after some time. When this happens periodically, the periodic heat release fluctuations will disturb the acoustic velocity field which in turn will periodically disturb the shear layer. This results in new vortices, thus closing the feedback loop. Secondly, these vortical structures can rapidly change the flame surface, which as discussed previously is also a pathway to thermoacoustic instabilities.

2.5 Mitigation techniques

The previously discussed Rayleigh criteria (25) suggests two possible ways to control thermoacoustic instabilities. First there is reducing the amplitude of p' or q' or adjusting the phase relation between them so that they are out of phase with each other (active measures). The other way is by increasing the acoustic loss term Φ so that it becomes larger than the acoustic source term (passive measures).

2.5.1 Active measures and passive measures

Active measures Active control techniques are utilized to minimize the combustion oscillations. It is an attractive strategy because it relies on modulation of system parameters like flow rates or by acoustic forcing instead of geometrical adjustments to the system as is the case with passive control measures [1]. Lots of research and experiments have therefore been done on laboratory scale setups, but it is not often found in industrial gas turbines. There are a few examples however, as Siemens for instance developed a feedback system that counteracts the instability found in one of their burners. A pressure sensor measured the pressure fluctuations and modulated the fuel flow rate through a control system to get rid of the noise [32].

Passive measures Passive control measures are mostly techniques where spatial changes are applied to the burner. Common examples are the addition of Helmholtz resonators, quarter wave tubes, baffles, flow liners, addition of pilot fuel or fuel staging. In the past, Siemens added a cylindrical extension, called the Cylindrical Burner Outlet (CBO), to the burner nozzle in one of their machines in order to push the time-lag between a pressure fluctuation at the fuel injection and the heat release fluctuation at the flame. This way the fluctuations are out of phase with each other. This, in combination with an asymmetric circumferential distribution in the annular combustion chamber successfully dampened the combustion instability [33].

The focus of this work will be on the effect of passive measures on the instabilities. Two mitigation techniques which are easily applied to the Siemens burner will be discussed in the next sections. Namely the Helmholtz resonators and fuel staging techniques.

2.5.2 Helmholtz resonators

As mentioned before, acoustic oscillations can be damped by using Helmholtz resonators or quarter-wave tubes. Both devices are basically cavities that are attached to the combustor, allowing flow from inside the combustor to enter them. The duct terminating in an open section shown in figure 2.4 is an example of such a quarter-wave tube. The resonance frequency of such ducts can only be changed by changing the length of the ducts, which can be prohibitive in certain geometries. Furthermore, these tubes can not be placed on the hot side of the combustion chamber, since it's not possible to purge them

with cooling air [4]. Therefore the focus in this section will be on Helmholtz resonators.

Damping mechanism of Helmholtz resonators The damping mechanism of Helmholtz resonators is primarily due to thermo-viscous losses. To explain this the resonators can be compared to mass-spring systems. When pressure in the burner oscillates, flow will enter and leave the resonator mouth. The flow in the neck can be seen as the moving mass, and the cavity of the resonator as the spring. At the resonance frequency, a large volume of fluid in the cavity compresses and expands, dissipating energy in the process and thus damping the acoustics [34].

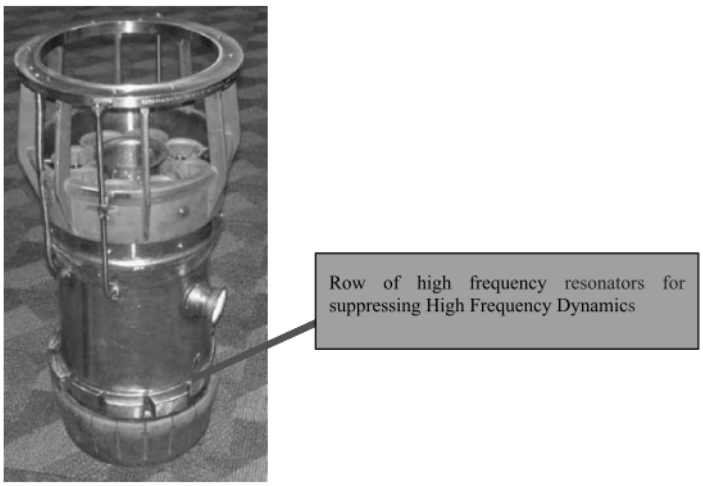

Figure 2.12: Example of High frequency dynamics resonators on a Siemens SGT6-5000F gas turbine burner [4].

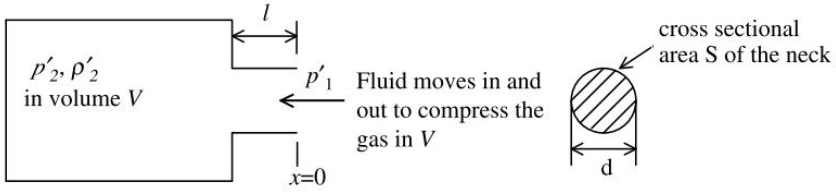

Figure 2.13: Schematic diagram of a Helmholtz resonator. Obtained from the work of Y. Huang and V. Yang [1].

An example of HFD resonators is given in figure 2.12. A schematic of a Helmholtz resonator is given in figure 2.13. The natural frequency f_0 of such a resonator assuming harmonic pressure and velocity fluctuations is given by equation (27). The viscous force and convection are neglected in this equation. Here c is the speed of sound inside the cavity, l the length of the neck, V the volume of the cavity and S the cross-sectional area of the neck.

$$f_0 = \frac{c}{2\pi}\sqrt{\frac{S}{Vl}} \tag{27}$$

The mass-spring-damper analogy will now be further explained as done in Huang and Yang [1]. Consider the mass spring system described by equation (28).

$$m\frac{d^2x}{dt^2} + R_D\frac{dx}{dt} + kx = F_d \tag{28}$$

Here m is the total mass of flow in the neck, x the displacement of that mass, R_D the mechanical resistance of the system, k the stiffness coefficient and $F_d = p'S$ the driving force which is the product pressure fluctuation from the combustor and the neck area. After dividing equation (28) by m and taking the time derivative of the equation, the following equation is obtained:

$$\frac{d^2u'}{dt^2} + 2\zeta\omega_0\frac{du'}{dt} + \omega_0^2 u' = \frac{d}{dt}\left(\frac{p'S}{m}\right) \tag{29}$$

with $\zeta = R_D/(2\omega_0 m)$ the damping coefficient and $\omega_0 = \sqrt{k/m}$ the natural frequency of the resonator. Using the definition of the impedance given in equation (17) and assuming harmonic oscillations for pressure $p' = \hat{p}e^{i\omega t}$ and velocity $u' = \hat{u}e^{i\omega t}$ as done in section 2.2, an expression for the impedance is obtained:

$$Z = R_a + i\chi = 2\zeta\omega_0\rho_0 l + i\frac{(\omega^2 - \omega_0^2)\,\rho_0 l}{\omega} \tag{30}$$

Rewriting equation (30) once more provides explicit equations for the acoustic resistance R_a and reactance χ:

$$R_a = \frac{R_D\rho_0 l}{m}, \quad \chi = 2\pi f\rho_0 l\left(1 - \frac{f_0^2}{f^2}\right) \tag{31}$$

Now the absorption coefficient α can be introduced. α is defined as the fraction of absorbed acoustic intensity of the wave going into the resonator. Recall equations (15) and (16), defining $\hat{f}$ and $\hat{g}$ as the incident and reflected wave respectively. Evaluating these equations at the interface resonator/combustor interface gives:

$$\hat{f} = \left(\frac{p' + u'\rho_0 c_0}{2}\right)_{x=0}, \quad \hat{g} = \left(\frac{p' + u'\rho_0 c_0}{2}\right)_{x=0} \tag{32}$$

Furthermore, the acoustic intensities of the incident en reflected wave are given by:

$$I_f = \frac{|\hat{f}|^2}{\rho_0 c_0}, \quad I_g = \frac{|\hat{g}|^2}{\rho_0 c_0} \tag{33}$$

The acoustic absorption coefficient α is given as:

$$\alpha = 1 - \frac{I_g}{I_f} = 1 - \frac{|\hat{g}|^2}{|\hat{f}|^2} \tag{34}$$

Finally, when substituting Eq. (32) into Eq. (34), the expression for the absorption coefficient becomes:

$$\alpha = \frac{4R_a\rho_0 c_0}{(R_a + \rho_0 c_0)^2 + \chi^2} \tag{35}$$

From equation 35 it can be seen that the maximum value for a fixed acoustic resistance R_a can be reached when the reactance χ goes to zero. This can be achieved by designing the resonator in such a way that its natural frequency is equal to that of the frequency of the oscillations that are to be damped, as can be seen in equation (31) [1][35].

Resonator considerations The resonators on the 8000H combustor have multiple resonator necks. Langfeldt et al. [36] proposed a new analytical model for Helmholtz resonators with multiple necks. They derived the general equation (36), where ρ is the density inside the cavity, S_i is the cross-sectional area of neck i and M_i the neck air volume mass. M_i is given by (37), where l_i and d_i are the neck height and diameter of neck i respectively. α_i is a end correction coefficient, which takes the inertia of a fluid around the neck into account [37].

$$f_0 = \frac{c}{2\pi}\sqrt{\frac{\rho}{V}\sum_{i=1}^{N}\frac{S_i}{M_i}} \tag{36}$$

$$M_i = \rho\left(l_i + \alpha_i d_i\right) \tag{37}$$

Several things are important to take into consideration when designing resonators. The resonance frequency needs to match that of the instability as stated before. Additionally, the ratio of resonator volume to combustor volume [38], the pressure loss coefficient which depends on neck geometry, the mass flow and the velocity through the neck [39] play roles in the performance. Furthermore, the location of the resonators on the burner plays a role, as the resonators should ideally be placed at the axial location of maximum heat release, since the flame is the source of the acoustic energy, and at the azimuthal locations of maximum pressure [4]. Lastly, resonators used in gas turbines are often purged with cooling air coming from the compressor. This of course also influences the damping performance. This purge air will enter the hot side of the combustor through the resonators, which could provide additional damping. The acoustic waves in the combustor interact with the flow at the resonator necks and vortices are shed, potentially further damping the instabilities [4].

Analytical solution All these considerations lead to the need of case-specific design and testing of the resonators to make sure they work as intended. Gysling et al. [38] characterized the effect of the resonators on the system by defining a transfer function as the frequency domain pressure ratio of combustor pressure to resonator pressure. This method will be used in this research and further explained in the methodology chapter

in section 3.6. To be able to validate simulation results of the transfer function, the analytical solution will be derived here.

Figure 2.13 shows the schematic of a Helmholtz resonator. The geometrical parameters used in the calculations are: cavity volume V, neck length l, neck diameter d and the cross sectional area of the neck S. Subscript 1 indicates quantities in front of the resonator neck, subscript 2 indicates quantities inside the resonator cavity and the subscript n indicates values inside the neck. First the continuity equation (1) is used. Furthermore, the assumption is made that the fluid moving into the neck causes adiabatic compression of the fluid in the cavity. This assumption makes it possible to eliminate the density perturbation ρ_2' from the equation. Applying the integral mass conservation law to the volume V of the cavity then yields equation (38), which states that the change of mass inside the cavity must be equal to the flux through the neck:

$$\frac{V}{c_0^2}\frac{dp_2'}{dt} = -\rho_0 u_n' S \tag{38}$$

Next, the resonator neck is assumed to be acoustically compact. This is justified because the neck length is much smaller than the wavelength of the acoustic mode. Compressibility effects can thus be neglected, and the integral momentum equation can be integrated along a streamline from a point inside the cavity to outside the resonator.

$$\rho_0 \frac{du_1'}{dt} Sl + \rho_0 S\left(u_1 u_1' - u_2 u_2'\right) = -S\left(p_1' - p_2'\right) \tag{39}$$

Due to seperation at the exit of the cavity, $u_1 \simeq 0$ during inflow into the cavity. Furthermore, $u_2' = u_n'$ due to the assumption that the neck is acoustically compact. Rewriting the momentum equation gives (40):

$$\rho_0 \frac{du_1'}{dt} l - \rho_0 - u_2 u_n' = p_2' - p_1' \tag{40}$$

where u_2 is the purge flow through the resonator. Now assuming harmonic oscillations for the pressure and velocity fluctuations:

$$u_n' = \hat{u}_n e^{-i\omega t}, \quad p_1' = \hat{p}_1 e^{-i\omega t}, \quad p_2' = \hat{p}_2 e^{-i\omega t} \tag{41}$$

Using equation (41) in the equations for mass (38) and momentum (40) and rewriting gives:

$$\hat{u}_n = \frac{V}{\rho_0 S c_0^2}\hat{p}_2 i\omega \tag{42}$$

$$-\rho_0 l \hat{u}_n i\omega - \rho_0 u_2 \hat{u}_2 = \hat{p}_2 - \hat{p}_1 \tag{43}$$

Now equations (42) and (43) can be combined to eliminate the velocity term $\hat{u}_n$ and get a relation for the pressure ratio $\frac{\hat{p}_1}{\hat{p}_2}$:

$$\frac{\hat{p}_1}{\hat{p}_2} = 1 - \frac{Vl}{Sc_0^2}\omega^2 + i\frac{Vu_2}{Sc_0^2}\omega \tag{44}$$

2.5.3 Fuel Staging

Another passive technique is fuel staging. This is commonly applied to can-combustion systems as a way to suppress oscillations [21]. Fuel staging involves injecting fuel at different locations throughout the combustor. Also the effect of fuel staging has to be evaluated per case as for instance is done in the work of Sewell et al. [40]. For a given turbine load, the total fuel mass flow rate is set, but the distribution between the fuel stages can be changed until there is a noticeable change in the flame dynamics. This is done step by step until the optimal split is found for a certain load. One approach which seems to damp oscillations quite well is staging the fuel in such a way that the symmetry of the injection is broken. This has been shown theoretically by Eisenhower et al. [41] and Noiray et al. [42], but also experimentally in the work of Cohen et al. [43] and D. James [44].

One way to utilize fuel staging as a mitigation technique is by changing the fuel air/ratio throughout the flame. Injecting different amounts of fuel at different premixers results in a flame with different temperatures throughout the flame. This makes the flame less coherent with the pressure fluctuations and the instabilities can be damped [45]. However, caution has to be taken when using this control technique, since it can have an adverse affect on the emissions [21]. The asymmetric fuel distribution leads to certain hot spots where more NO_x is produced than in the case of a uniform flame temperature distribution. In addition to not meeting NO_x regulations, the hot spots also have a negative effect on the material lifetime of the combustor.

2.6 Computational fluid dynamics

The main analysis approach in this work will be Computational Fluid Dynamics (CFD). It has additional advantages over acoustic code solvers to study thermoacoustic instabilities. Since Helmholtz solvers are based on linear approximations, they can only predict a mode shape and the growth rate of the mode, but no information about the processes that actually happen when the system is unstable. CFD solves the governing equations of fluid dynamics, which were given in section 2.1. These equations are discretized and solved numerically. The three most common levels of CFD given in order from least to most computationally demanding are: Reynolds Averaged Navier Stokes (RANS), Large Eddy Simulations (LES) and Direct Numerical Simulation (DNS).

- In RANS, only the mean flow fields are resolved and no temporal information is obtained. This also means that no instantaneous turbulence effects are captured. A variation of RANS exists, namely Unsteady RANS or URANS.
- DNS solves the Navier Stokes equations directly and thus fully captures turbulence. However, this means that DNS also has to describe the smallest scales of turbulence and the inner instantaneous structure of the flame front, leading to the requirement of a very fine grid [14].
- Lastly there is LES, which sits somewhere between RANS and DNS. Unlike DNS, LES does not intend to solve all turbulent scales, but as the name implies only the large eddies, which contain most of the turbulent energy [9]. Since LES is an unsteady solver, also information about the instabilities themselves can be obtained, in contrast to linear Helmholtz solvers.

Figure 2.14 illustrates the difference between the three methods. For modeling of thermoacoustic combustion instabilities, URANS and LES can both be used. Even though URANS is computationally less expensive than LES and capable of capturing main thermoacoustic effects, it is unable to capture the interaction between the acoustics and the turbulence, since all turbulence is modeled in URANS. LES is therefore more popular in thermoacoustic studies and will be used in this work [46]. In the next sections RANS and LES will be discussed further since they will be used in this research. Afterwards the reacting flow models used in the simulations will be discussed in detail in section 2.6.3

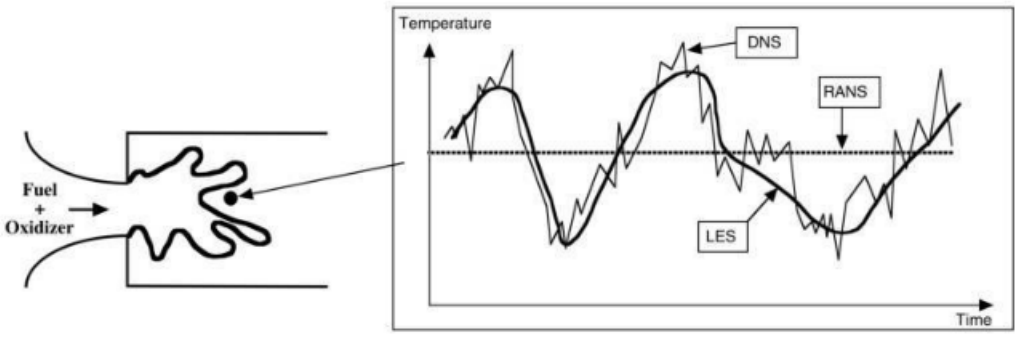

Figure 2.14: Time signal of local temperature computed with RANS, LES and DNS in a turbulent flame to illustrate the different solutions obtained. From the work of Poinsot [14]

2.6.1 RANS

Reynolds Averaged Navier Stokes equations are obtained by assuming every instantaneous solution quantity Φ like velocity, pressure, energy or species concentration can be decomposed into a mean value $\bar{\Phi}$ a fluctuation around this value Φ'. This is called a Reynolds decomposition and as seen in equation 45. This decomposition is inserted in the Navier Stokes equations and these equations are then averaged to obtain the RANS equations 46 and 47.

$$\Phi = \bar{\Phi} + \Phi' \tag{45}$$

$$\frac{\partial \bar{\rho}}{\partial t} + \frac{\partial \overline{\rho u_i}}{\partial x_i} = 0 \tag{46}$$

$$\bar{\rho}\frac{\partial \bar{u_j}}{\partial t} + \frac{\partial}{\partial x_j}\left(\bar{\rho}\bar{u_i}\bar{u_j} + \bar{\rho}\overline{u_i' u_j'}\right) = -\frac{\partial \bar{p}}{\partial x_i} + \frac{\partial \bar{\tau}_{ij}}{\partial x_j} \tag{47}$$

The RANS equations contain a new term in the momentum equation (47), called the Reynolds Stress $\overline{u_i' u_j'}$, and a similar term for the energy equation $\overline{u_j' T'}$. These terms originate from the nonlinear advection terms in the Navier Stokes and energy equation. Since these are new unknown quantities, a closure problem occurs and different models have been developed to solve these terms [7]. Common closure models are based on the Boussinesq closure hypothesis. This closure hypothesis is based on the analogy between the turbulent stress tensor $-\rho\overline{u_i' u_j'}$ found in the RANS equation and the molecular stress tensor $\sigma_{ij} = -p\delta_{ij} + \tau_{ij}$. Examples of these models are the $k-\epsilon$ [47] or $k-\omega$ [48] models. Other models are based on the Reynolds Stress Transport Equation [49]. The $k-\epsilon$ and $k-\omega$ models are two-equation models which perform generally well. $k-\epsilon$ works pretty well for most applications but is less accurate for the viscous near-wall region than the $k-\omega$ model. The downside of the $k-\omega$ model is that its boundary layer computations are very sensitive to free-stream values of ω, in turn making the model very sensitive to inlet boundary conditions for internal flows [48].

Since RANS is computationally cheap, it will be used to obtain a first solution of the flow field in the combustor which will then be used as an initial condition for the Large Eddy Simulations to save time. Additionally, RANS will be used to select a suitable value for the Turbulent Flame Speed rate coefficient A, which will be discussed in section 2.6.3.

2.6.2 LES

As mentioned previously, Large Eddy Simulations focus on solving the large eddies and modeling the smaller eddies. This is done by applying a filter instead of averaging like with RANS. First the assumption is made that a solution quantity Φ can be decomposed as in equation (48). Here $\tilde{\Phi}$ is the filtered value and Φ the sub-filtered or sub-grid value. There are two ways of filtering; explicit and implicit filtering. The classical way of filtering is the explicit form, where a chosen filter function is applied to the Navier-Stokes equations. Any filtered variable $\tilde{\Phi}$ is defined as in (49), where $G(\mathbf{x}, \Delta)$ is the selected

low-pass convolution filter function and Δ the filter width. The advantages of using an explicit filter is that the filter shape is well defined and the truncation error is relatively small [50].

$$\Phi = \tilde{\Phi} + \Phi' \tag{48}$$

$$\tilde{\Phi}(\mathbf{x}, t) = \int \int \int_{-\infty}^{\infty} G(\mathbf{x} - \mathbf{x}', \Delta)\Phi(\mathbf{x}', t)d\mathbf{x}' \tag{49}$$

In the CFD software STAR-CCM+, which will be used for the simulations, implicit filtering is applied. Instead of specifying both the filter shape $G(\mathbf{x}, \Delta)$ and filter width Δ, only the filter width is specified. The grid cell size is dictates the filter width, meaning the assumption is made that the subgrid-scale eddies are smaller than the cell sizes in the domain [51]. The advantage of this is that the LES takes full advantage of the grid resolution cutting down the computation cost. The disadvantages are that the filter shape is unknown and the truncation error can be large if the mesh is not fine enough [50]. Figure 2.15 helps to visualize the filtering procedure. Eddies smaller than the mesh are modeled

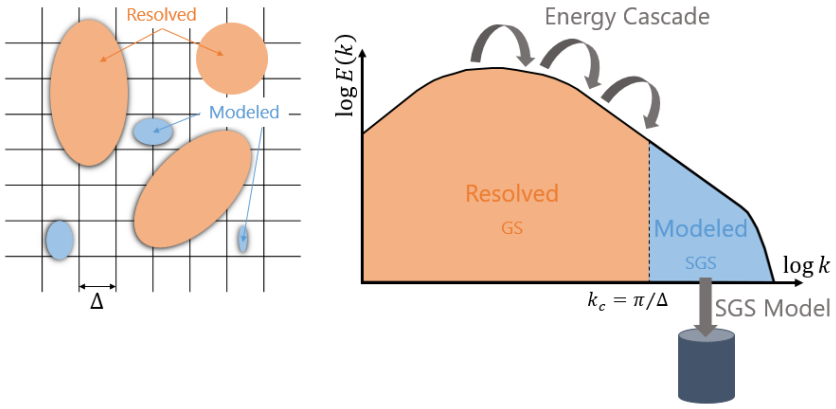

Figure 2.15: Eddies larger than the mesh size (orange) are directly resolved and eddies equal to or smaller than the mesh size (blue) are modeled [52].

After inserting the decomposed quantities (48) into the NS equations, the filtered Navier-Stokes equations are obtained:

$$\frac{\partial \tilde{u}_i}{\partial t} + \frac{\partial \tilde{u}_i \tilde{u}_j}{\partial x_j} = \frac{1}{\rho_0}\frac{\partial \tilde{p}}{\partial x_i} + \frac{\partial}{\partial x_j}\nu\left(\frac{\partial \tilde{u}_i}{\partial x_j} + \frac{\partial \tilde{u}_j}{\partial x_i}\right) + \frac{1}{\rho_0}\frac{\partial \tau_{sgs}}{\partial x_j} \tag{50}$$

A new term called the subgrid stress τ_{sgs} is introduced. It is defined as in equation (51). The subgrid stress term accounts for the effective stress applied to the macrostructure by the scales from the microstructure eddies which are filtered out. The subgrid stress contains a new unknown quantity $\widetilde{u_i u_j}$, which also requires modeling. The difference between the subgrid stress and the Reynolds stress is that the Reynolds Stress describes the stress on the flow due all turbulent structures, while the subgrid stress describes only the stress of the microstructure [7].

$$\tau_{sgs} = -\rho_0 \left(\widetilde{u_i u_j} - \tilde{u}_i \tilde{u}_j \right) \tag{51}$$

The earliest subgrid-scale (SGS) model used is the Smagorinsky SGS model [53] which is the basis of a lot of advanced models. This model has two big shortcomings. Firstly, it contains a model coefficient which is not universal for every flow and needs to be tuned accordingly. Secondly, the model performed poorly near walls, since it gave non-zero values for the subgrid-scale velocities, even though all turbulent fluctuations are damped near the walls. Therefore often damping functions are combined with the Smagorinsky SGS model [54]. A more modern model called the Wall-Adapting Local-Eddy Viscosity (WALE) model was proposed by F. Nicoud and F. Ducros [55] in 1999 which does not have the shortcomings of the Smagorinsky model. Additional advantages of this model are its applicability to complex geometries because it only uses local information. The WALE model is thus used for the SGS modeling in this research.

2.6.3 Reacting flow model

During combustion of fuel and oxidizer, a large number of species are reacting with each other in an even larger number of reactions. These reactions happen in a very short time and the interaction of turbulence with these reactions makes it even more complex. CFD simulations for solving equation (3) for every species involved in the combustion process would be unfeasible for LES. Two branches of combustion modeling in CFD can be identified. Reacting species transport and tabulated flamelet models. In reacting species transport models a reduced reaction mechanism scheme involving less species and reactions is used and the model solves the conservation equation (3) for each of these species in the mechanism. These models are computationally more demanding than the flamelet models and are useful when chemical kinetic phenomena like slowly forming pollutants, flame position or prediction of ignition/extinction are of interest [56]. Since this is not the focus of this work, the other option will be further discussed. In flamelet models, the reacting flow is parameterized by a limited number of variables which describe the thermodynamic state of the flame. Instead of solving the transport equations for the provided species, a limited number of transport equations is solved for the variables belonging to the flamelet model.

Flamelet Generated Manifold Flamelet models are based around the assumption that a turbulent flame can be approximated as an ensemble of laminar flamelets (basic 1D laminar flames). The turbulent flame is seen as a laminar flame embedded in an otherwise non-reacting turbulent flow field. This assumption is valid for the purpose of gas turbine combustion, as the combustion happens in the corrugated flamelets regime in the Borghi diagram 2.3 as discussed in section 2.1.3. A lookup table is generated before the simulation, storing relevant quantities like mass fractions and reaction rates as a function of a set of independent variable which are dependent on the flamelet model selected.
The flamelet model chosen for this work is the Flamelet Generated Manifold (FGM) model [57]. For this model, the independent variables on which the computed thermo-

chemistry depends are: mixture fraction Z, progress variable y and enthalpy h. Z and y are given in equations (52) and (53). Here m_f and m_{ox} are the mass of fuel and mass of oxidizer respectively. The progress variable is used to track the reaction front or flame front and is computed using species weight W_k the species mass fraction Y_k.

$$Z = \frac{m_f}{m_{ox} + m_f} \tag{52}$$

$$y = \sum (W_k Y_k) \tag{53}$$

A lookup table is generated based on the reaction mechanism, pressure and initial temperature provided by the user. The dimensions of the table depend on the number of independent variables. Then the simulation can take place. At each iteration the transport equations for the independent variables are solved. As an example, the transport equation of the progress variable is given (54). The transport equations for the Z and h are similar with the exception that the RHS of those equations is zero.

$$\frac{\partial \rho y}{\partial t} + \boldsymbol{\nabla} \cdot (\rho \mathbf{u} y) - \boldsymbol{\nabla} \cdot (\Gamma_y \boldsymbol{\nabla} y) = \dot{\omega}_y \tag{54}$$

After solving the transport equation, all other relevant flame properties like temperature can then be taken from the generated table.

Flame Propagation model The non-zero source term in the progress variable transport equation needs to be modeled. This source term accounts for the coupling of chemistry and turbulence. The model used for this is the Turbulent Flame Speed Closure (TFC) model. The flame front propagates at the turbulent flame speed, which in the case of this model is given by an algebraic equation (55), where A is the TFC rate coefficient, ρ_u the unburnt density, y the progress variable, and S_t the turbulent flame speed.

$$\dot{\omega}_y = A \rho_u S_t |\boldsymbol{\nabla} y| \tag{55}$$

As stated in section 2.1.3, different models exist to estimate the turbulent flame speed. The model used in this work is the Zimont turbulent flame speed correlation [58] as given in equation (56). Here G is the stretch factor, u' the subgrid-scale velocity fluctuations, α_u the unburnt thermal diffusivity of the unburnt mixture, I_l the integral turbulent length scale.

$$S_t = \frac{1}{2} G \left(u'\right)^{\frac{3}{4}} S_l^{\frac{1}{2}} \alpha_u^{-\frac{1}{4}} I_l^{\frac{1}{4}} \tag{56}$$

The laminar flame speed S_l is computed with the Gülder correlation [59] as given in equation (57). Here Z, W, η, ξ, α and β are fuel dependent constants. As stated in section 2.1.3, the laminar flame speed in premixed combustion further only depends on the equivalence ratio ϕ, unburnt temperature T_u and the pressure p.

$$S_l = Z W \phi^{\eta} e^{-\xi(\phi - 1.075)^2} \left(\frac{T_u}{T_0}\right)^{\alpha} \left(\frac{p}{P_0}\right)^{\beta} \tag{57}$$

3 3D numerical setup of baseline case

In this chapter the approach to setting up the baseline CFD simulation is given in section 3.1. The first RANS and LES results will be given in sections 3.2 and 3.3. Afterwards, the data acquisition approaches are given in sections 3.4 through 3.6

3.1 Simulation setup

3.1.1 Geometry

The burner used in the simulations is the combustor of the 8000H gas turbines. A schematic overview of this burner is given in figure 3.1. Depending on the turbine model, either 12 or 16 burners are used. For the purpose of this research only one burner is simulated. Compressed air enters from the compressor and goes through the flow sleeve (3). There it mixes with fuel injected through the pilot burner (2) and the 8 main burners (1). The mixture is burned and the flame ankers on the pilot cone. The hot burned gas is guided through the burner through the liner (4) and the transition piece (5) to eventually reach the turbine vanes to generate power. To mimic the termination in the DLR rig and save computation cost, stationary turbine vanes are used for the termination instead of rotating ones. Additionally, an orifice is placed behind these vanes to reduce IFD.

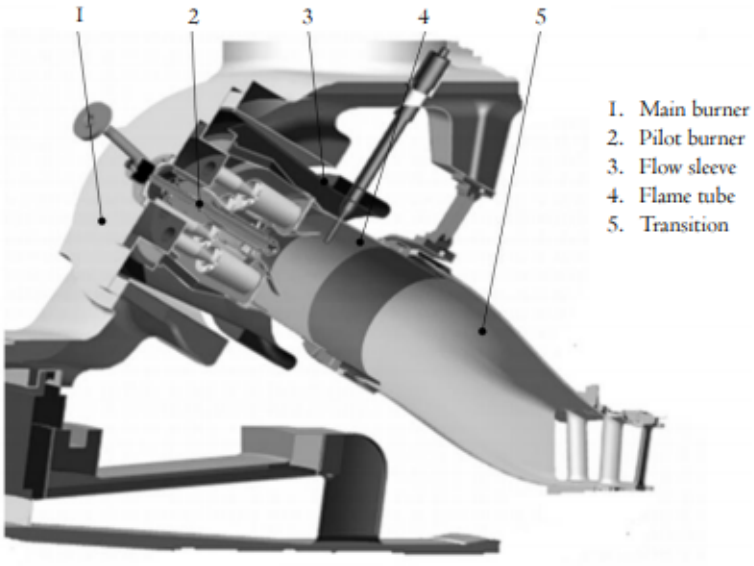

Figure 3.1: Schematic overview of the 8000H combustor [60]

3.1.2 Mesh

When generating the mesh, different criteria have to be taken into account. To save computation time, the overall cell count is required to be small, while still providing accurate solutions. The mesh type and quality criteria taken into account will be briefly discussed in this section.

Table 3.1: General mesh settings

Setting	Value
Number of cells with resonators	31.6 million
Number of cells without resonators	29.9 million
General cell size	15 mm
Number of prism layers	3
Cell size in resonator holes	1.5 mm
Cell size in fuel injectors	2.5 mm
Cell size in flame region	8 mm

Mesh type Mesh generation is done with STAR-CCM+. As seen in figure 3.1, the burner has a quite complex geometry. Therefore a unstructured mesh is required. The chosen mesh type is the unstructured polyhedral mesh, which is relatively easy to build and provides a balanced solution for complex geometries like this one [56]. General mesh settings are used for the bulk of the mesh, and further controlled refinements are used for critical areas like injector holes, the flame region or boundaries.
General mesh settings are given in table 3.1 and a cross-section overview of the complete mesh is given in figure 3.2.

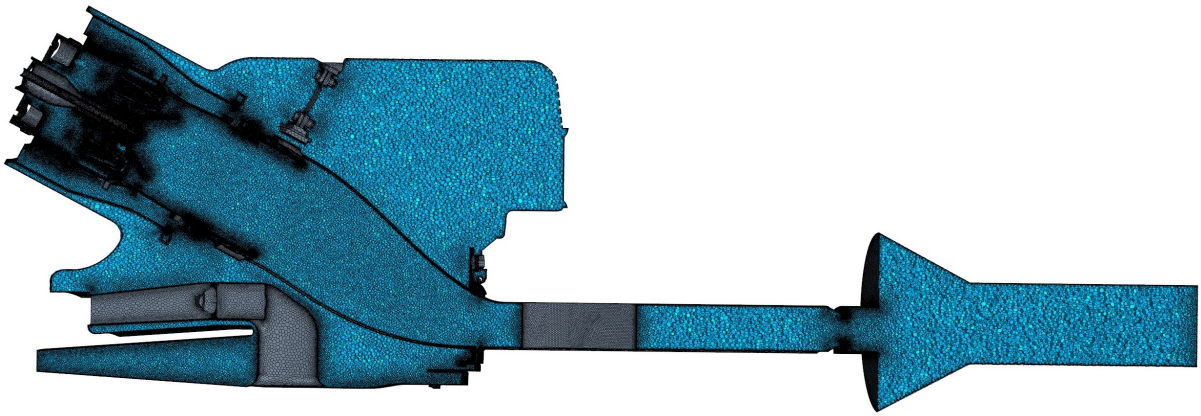

Figure 3.2: Midplane cross-section of the polyhedral mesh.

Pope criteria In order to determine whether the LES is resolving enough turbulence and to check if the mesh is not too coarse, the ratio of subgrid-scale turbulent kinetic energy to the total turbulent kinetic energy is measured. This ratio M is defined in (58).

$$M = \frac{k_{sgs}}{k_{sgs} + k_{res}}, \qquad k_{res} = \frac{1}{2}\langle(\tilde{u}_i - \langle\tilde{u}_i\rangle_T)\,(\tilde{u}_i - \langle\tilde{u}_i\rangle_T)\rangle_T \tag{58}$$

where k_{sgs} denotes the SGS turbulent kinetic energy, k_{res} the resolved kinetic energy. $\langle\rangle_T$ the temporal average (mean velocity field) and u_i the instantaneous velocity field. A value of 1 corresponds to a RANS simulation and indicates poor resolution for a coarse

mesh. A value of 0 corresponds to DNS and indicates that the flow is very well resolved. The resolved turbulent kinetic energy can be estimated through field variance values of the three velocity components. A mean value of 0.1 was attained for the whole domain. The highest mean value of M in the combustion region reaches 0.3, which is deemed sufficient.

Courant number The second criterion taken into account is the CFL condition. This condition states that the Courant number should not exceed a certain maximum value. Two variations are considered, namely the convective Courant number given in equation (59) and the acoustic Courant number given in equation (60).

$$Co = \frac{|u|\Delta t}{\Delta x} \tag{59}$$

$$ACFL = \frac{(|u| + c)\Delta t}{\Delta x} \tag{60}$$

The Courant number depends on the mesh size, chosen time step and convective velocity. To ensure a converging solution for LES, the Courant number should not be larger than unity [56]. The acoustic Courant number depends on the mesh size, chosen time step and the sum of the convective velocity and speed of sound. To ensure minimal dispersion and dissipation of acoustic waves, $ACFL < 0.7$ should be maintained [61].

Cells per wavelength The last consideration is the cells per wavelength. H. Krediet has researched the dissipation and dispersion of acoustic waves depending on the number of cells per wavelength. The wavelength of an acoustic wave is defined as $\lambda = \frac{c_0}{f}$. The number of cells per wavelength achieved for the mode of interest is $n = 30$. According to the results in the work of H. Krediet [61], the amount of numerical dispersion and dissipation of acoustic waves at $ACFL = 0.7$ is within acceptable range with 30 cells per wavelength.

Table 3.2: Summary of mesh criteria values

Criteria	Region	Value
Average Pope (M)	Whole domain	0.1
Highest Pope (M)	Flame Region	0.28
ACFL	Pilot cone	0.6
ACFL	Liner walls	0.6
Cells per wavelength	Flame region	30

3.1.3 Boundary conditions

The same boundary conditions have been used for the RANS and the LES. An overview of the different boundary conditions types will be given in the next part. All walls in the

domain are adiabatic walls since perfect heat transfer modeling is not the focus of this study.

Fuel inlets The fuel used in the simulations is pure methane and it is injected through 5 different inlets. There are eight swirlers providing the bulk of the fuel inflow, positioned in a circle as seen in figure 3.1. For tunability they are divided in two sets of four; namely A and B stage fuel. Before the compressor air reaches the main swirlers to mix with the fuel, already a small amount of fuel is injected from the C-stage to further help the premixing, reducing the chance of flashback. Lastly, the P- and D-stage fuel provides fuel in the middle of the flame to help start up and stabilization of the flame in the pilot cone. One of the mitigation techniques discussed in chapter 2 is fuel staging. Different fuel distributions could amplify or reduce the HFD in the burner. To that end, two different fuel distributions will be used in the simulation. The distributions are characterized by the *AB bias*, as given in Eq. (61), where $\dot{m}_A$ and $\dot{m}_B$ are the total fuel mass flow going to the A- and B-stage respectively. The inlet boundary conditions are mass flow boundary type.

$$AB\ bias = \frac{\dot{m}_B}{\dot{m}_A} \tag{61}$$

Oxidizer inlet The bulk of the air inlet is coming straight from the compressor. Two additional small inlets are added to mimic real life leakages. One inlet is found at exit of the transition piece or entrance of the turbine vanes. The other inlet is found at the spring clip which connects the end of the liner with the beginning of the transition piece. The burner operates at part load because this operating regime tends to be the most unstable. The compressed air is therefor at a medium pressure level. The inlet boundary conditions are of the mass flow boundary type.

Outlet An important part of successfully finding the acoustic mode of interest is choosing the correct outlet type for the simulation. A poor choice of outlet type may reduce the amplitude of the HFD or even suppress its occurrence completely [14].

The standard pressure outlet is robust and simple, but acoustically inappropriate for compressible flows. Normally, the pressure in the domain is maintained at the predefined pressure p_∞ by means of waves conveyed from outside the domain into the domain through the outlet. When the local pressure p is different from the set pressure p_∞, a reflected wave is produced to bring the local pressure closer to the set pressure [14]. STAR-CCM+ offers a Non-reflective boundary condition (NRBC), which is used instead. NRBC allow for waves to travel out of the domain without introducing reflective waves to counteract the pressure drift. A perfectly non-reflective outlet would result in a large pressure drift away from the set pressure. Therefore the NRBC can be tuned to allow for some degree of reflection in order to try and maintain the set pressure.

3.1.4 Numerical Settings

The numerical schemes chosen for the simulations are based on the work of Thomas Indlekofer [62], who researched the predictive capabilities of thermoacoustic instabilities using STAR-CCM+. Different numerical schemes were tested on a convecting vortex and traveling acoustic wave to determine the amount of numerical dispersion and dissipation. Table 3.3 shows the settings used for the simulations. These are settings are based on Indlekofer's results, STAR-CCM+ documentation recommendations and selected to balance accuracy and computation time.

Table 3.3: Overview of numerical settings for the large eddy simulations

LES Settings	
Time Scheme	Implicit Unsteady
Temporal Discretization	Second-Order Backward Difference
Spatial Discretization	Bounded Central Differencing
Coupled/Segregated	Segregated
Timestep	5e-6 s
Inner iterations	8
Simulation runtime	0.25 s
SGS Turbulence model	WALE
Reacting flow model	FGM
Flame propagation model	TFC

3.2 RANS

As stated before, a RANS simulation will be ran first to use as an initial condition for the LES. Additionally, RANS will be used to find a good initial value for the TFC rate coefficient A.

3.2.1 TFC rate coefficient study

Since the simulations are done at part load, no OH* chemiluminescence data is available. There are thermal paint images available for this operating condition, but matching them to the temperatures in the simulation would still leave some uncertainty due to the adiabatic walls assumption in the simulation. Since the goal of this research is to obtain thermoacoustic instability data, the exact position of the flame should not be too constraining if within acceptable range of the real flame. A design study is done, running the RANS with different values of A starting from Design Number 1 with $A = 0.5$ to Design number 9 with $A = 2.5$ in steps of 0.5. On one hand, the flame should have no flashback into the premixing duct, and on the other hand no unburnt fuel should be entering turbine section. The mass flow rate at the interface between the transition piece and turbine section is monitored and the results are plotted in figure 3.3. Additional figures of the progress variable and surface temperatures can be found in appendix A.1.

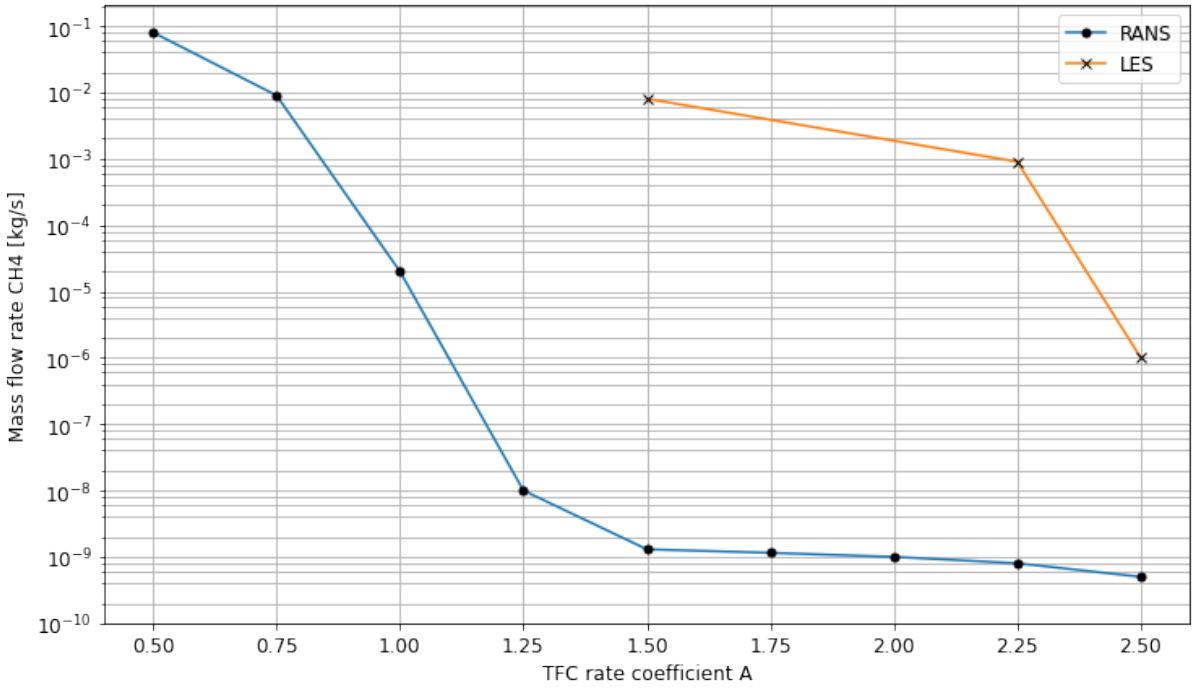

Figure 3.3: Mass flow rate of CH4 entering the turbine section of the domain in the RANS simulation (blue line) and LES (orange line) for different TFC rate coefficients A.

Based on the results in figure 3.3 and in appendix A.1, the RANS simulation with the TFC rate coefficient of $A = 1.5$ will be used as an initial condition for the LES. The resulting flame is visualized in figure 3.4

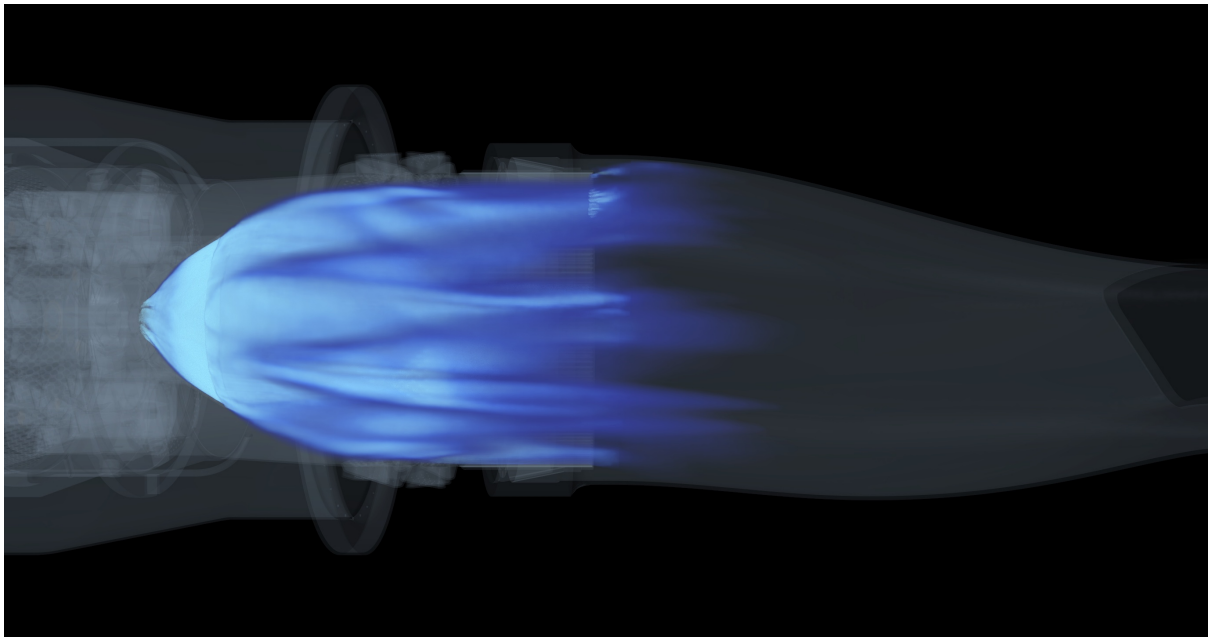

Figure 3.4: Chemistry Heat Release of RANS case flame

3.3 LES

3.3.1 Solution flow field

After running the LES, it became apparent that the flame looks different when switching from RANS, even though the same TFC rate coefficient is used. This becomes clear when comparing figure 3.4 with the left image in figure 3.5. This is to be expected since even though the same model is used for both simulations, RANS and LES are fundamentally different. When looking at the formulation of the TFC model as given in section 2.6.3, it becomes clear that a lot of parameters are dependent on the type of simulation ran. LES resolves the fluctuations and values provided to the turbulent flame speed correlation Eq. (56) can therefor differ a lot from the RANS simulation.

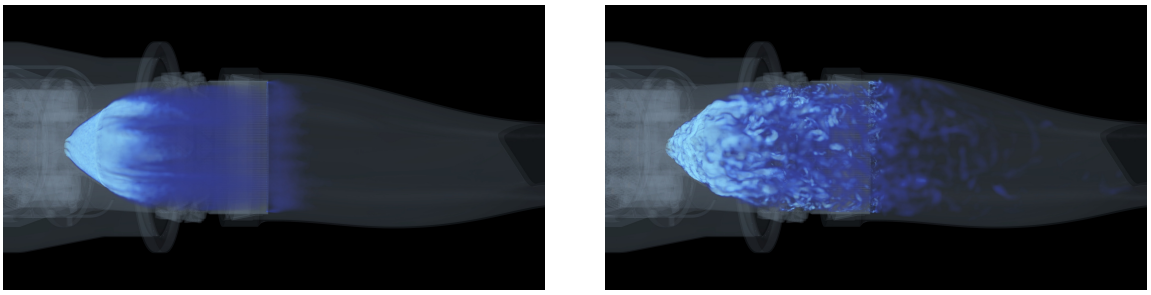

Figure 3.5: Mean (left) and Instantaneous (right) Chemistry Heat Release of the LES case flame with TFC Rate Coefficient of $A = 1.5$

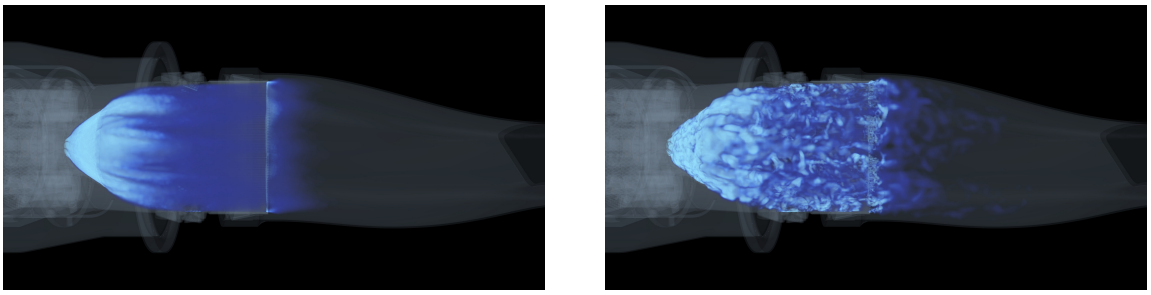

Figure 3.6: Mean (left) and Instantaneous (right) Chemistry Heat Release of the LES case flame with TFC Rate Coefficient of $A = 2.25$

Differences RANS and LES Many combustion modeling approaches for RANS and LES are similar due to the fact that combustion takes place at unresolved scales. Both RANS and LES have time and length scales that are related through the nature of turbulence. However, care must be taken when interpreting the different meaning of seemingly similar quantities [63]. This is also the case with the Zimont turbulent flame speed correlation Eq. (56). The biggest difference is likely due to the u' term in this correlation. For RANS simulations, this term is calculated as the RMS velocity fluctuations, while for LES simulations this is the grid size dependent sub-grid scale velocity fluctuation. Further decreasing the cell size in the flame region would result in more scales being

resolved and smaller sized eddies being modeled, thus having smaller values of u' used in the flame speed calculation and finally resulting in a lower turbulent burning velocity. The integral turbulent length scale I_l is also strongly dependent on the simulation type. For RANS, the $k-\omega$ model is used, which defines the turbulent length scale as

$$I_l = \tau_t k^{1/2} \tag{62}$$

where the k is the modeled turbulent kinetic energy and τ_t the turbulent timescale which is defined as

$$\tau_t = (\beta^* \omega)^{-1} \tag{63}$$

Here ω is the modeled specific dissipation rate and β^* a model coefficient.
For LES the turbulent length and timescale are defined as

$$I_l = \tau_t \sqrt{C_t \frac{\mu_t}{\rho} S} \tag{64}$$

$$\tau_t = \frac{C_t}{S} \tag{65}$$

Here C_t is a model coefficient, μ_t the modeled subgrid scale turbulent eddy viscosity, ρ the local density and S the modulus of the mean strain rate tensor which is solved from the resolved velocity field.

$$S = |\mathbf{S}| = \sqrt{2\mathbf{S} : \mathbf{S}^T}, \quad \mathbf{S} = \frac{1}{2}\left(\boldsymbol{\nabla}\widetilde{\mathbf{u}} + \boldsymbol{\nabla}\widetilde{\mathbf{u}}^T\right) \tag{66}$$

There are large differences in the quantities used for the models [64] and very few studies available addressing the comparison of RANS and LES methods for reacting flow in complex configurations [65]. Since this falls out of the scope of this work, the differences will not be further explored. Instead, the reasoning for the choice of the TFC rate coefficient for the rest of the simulations will be given in the next paragraph.

Final TFC rate coefficient The mass flow rate of CH4 entering the turbine section for the LES case is in the order of 1e-2 kg/s, coming close to design number 2 in figure 3.3 which corresponds to a RANS simulation with a TFC rate coefficient of 0.75. When taking a closer look at the instantaneous snapshot of the flame in figure 3.5, small detached flames can be seen towards the transition exit. This image confirms that the combustion regime is indeed that of Corrugated flamelets as discussed in section 2.1.3.

Due to the differences between RANS and LES, the TFC rate coefficient of 1.5 in LES showed a CH4 mass flow rate equal to that of a RANS simulation with a TFC rate coefficient of 0.75. Because of this, it was decided to increase the coefficient by 0.75 to $A = 2.25$. The new flame is visible in figure 3.6.

After further increasing the coefficient, the CH4 mass flow rate at the exhaust plane decreased to 1e-3 kg/s, which is a negligible fraction of the total fuel mass flow. The

detached flames are still visible but do not move as far into the burner, implying more efficient burning. Furthermore, increasing A to 2.5 resulted in flame flashback. Most importantly, strong signs of HFD were captured with the LES with $A = 2.25$, as will be shown in section 4.1. Taking these considerations into account, the value of 2.25 is chosen for all further simulations.

3.4 Thermoacoustic instability data acquisition

To record the occurrence of HFD, pressure probes have been placed around the flame near the walls of the combustor. The probes are located there since the pressure amplitude is most likely the highest near the walls since the velocity tends to zero as show in figures 2.5.

The first set of probes is on the walls at the axial location of the pilot cone. The second set of probes is placed between the pilot cone and the resonators and the last set is placed right before the resonators. Additionally, pressure probes have been placed inside the fuel lines to check if the equivalence ratio driving mechanism discussed in section 2.4 could be the cause of the HFD.

After obtaining the pressure signals from the simulation, the frequency spectrum is obtained from these pressure signals by means of Fourier analysis. The peaks of the spectra will be compared against the spectra of the DLR experiments to see if the HFD instability mode found in the DLR experiments also exists in the simulation. Finally, spectrograms are made from the signals to see when the HFD occurs within the simulation. Results of this approach will be discussed in section 4.1.

Cross power spectral density and phase To check how much the pressure and heat release interact with each other, quantities like the cross power spectral density (CPSD), its phase and the coherence will be computed. They will be briefly discussed next.

The cross power spectral density (CPSD) is the FFT of the cross-correlation $r_{xy}(\tau)$ of two time signals $x(t)$ and $y(t)$. In this analysis $x(t)$ and $y(t)$ are the heat release and pressure fluctuations respectively. The cross correlation is computed by multiplying the signals at each point in time and summing up the products. It is defined as:

$$r_{xy}(\tau) = \int_{-\infty}^{\infty} x(t+\tau)y(\tau)d(\tau) \tag{67}$$

The power spectral density shows how the power of a signal is distributed over the different frequencies and has units power per Hertz. It tells whether frequency components in $x(t)$ are associated with large or small amplitudes at the same frequency in $y(t)$ [66]. It returns a complex number with a real and imaginary part. The magnitude of the CPSD shows at which frequencies most power is located, and the angle of the CPSD gives the phase between the two signals. The CPSD is defined as:

$$P_{xy}(\omega) = \int_{-\infty}^{\infty} r_{xy}(\tau)e^{-i\omega\tau}d\tau \tag{68}$$

Lastly the coherence will be discussed. The coherence of two signals shows the extent of how much signals $x(t)$ and $y(t)$ are linearly related, or in other words, how much of the power response of signal $y(t)$ is caused by the input signal $x(t)$ [67]. The coherence is a value between zero and unity. The coherence is defined as the squared magnitude of the CPSD normalized by the auto power density spectra of the individual signals:

$$C_{xy} = \frac{|P_{xy}(\omega)|^2}{P_{xx}(\omega)P_{yy}(\omega)} \tag{69}$$

3.5 Center of heat release monitoring

To attempt to track the effect of HFD on the flame, the center of heat release can be tracked during an HFD event. Since the flame is large and the mode could affect different parts of the flame in a different way, the combustion chamber is divided into cell sets. This way the flame is discretized and the center of heat release can be computed for every cell set. Figure 3.7 shows an overview of the cell sets. The flame region is divided into 5 axial bins and 8 tangential bins per axial bin, totaling 40 cell sets. The 8 tangential bins are positioned directly downstream and in front of the main swirlers. An overview of the cell sets is given in figure 3.7. The center of heat release for every cell set is computed similar to how the center of mass is calculated as shown in equation 70:

$$\vec{X}_{CoHR} = \frac{\int_V \vec{x} \cdot q\left(\vec{x}\right) dV}{\int_V q\left(\vec{x}\right) dV} \tag{70}$$

where $\vec{x} = (r, \theta, z)$ is the distance vector. This distance vector is multiplied with the spatially dependent heat release $q\left(\vec{x}\right)$ and integrated over the volume V. This is then divided by the volume integral of only the heat release to obtain the vector $\vec{X}_{CoHR}$ which contains the polar coordinates of the center of heat release [17].

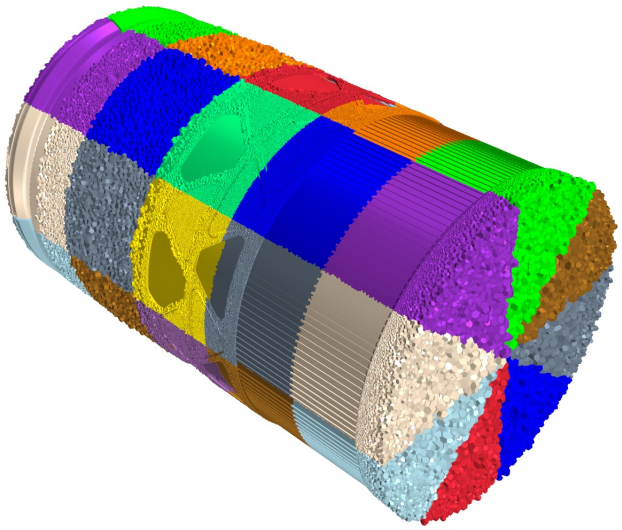

Figure 3.7: Overview of the 40 cell sets used to compute the center of heat release of the flame during the simulations.

Every cell set contains pressure probes so that the interaction between the local pressure and local heat release fluctuations can be analyzed This is done in section 4.1.2.

3.6 Resonator transfer functions

In order to capture the behavior of the different resonators, a frequency response transfer function analysis similar to the one in Gysling et al. [38] is done. The pressure inside the resonator cavity and in front of the resonator on the hot side of the combustor is recorded. An example of the probe location is visible in figure 3.8. Welch's method is used to convert the data to the frequency domain. The Transfer Function is defined as in equation 71.

$$TF = \frac{\hat{S}^W_{in}}{\hat{S}^W_{out}} \tag{71}$$

where $\hat{S}^W_{in}$ and $\hat{S}^W_{out}$ are the Welch estimate of the power spectral density of the pressure inside and in front of the resonator respectively.

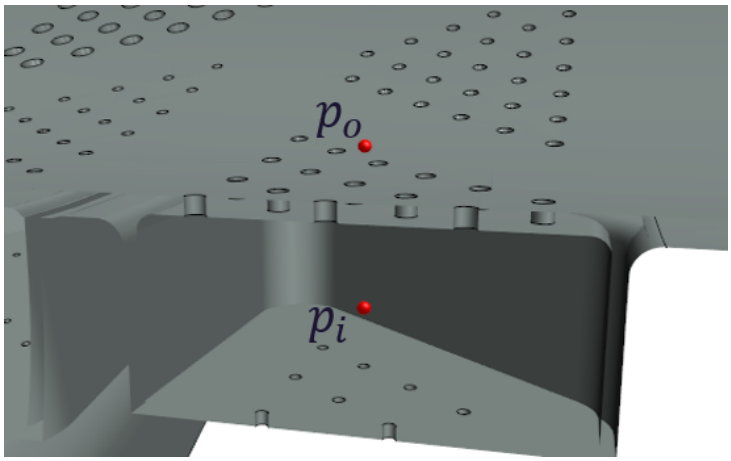

Figure 3.8: Example of pressure probe locations. p_i is the pressure inside the resonator cavity, p_o the pressure outside the resonator.

4 Case comparison results and discussion

Four different simulations are ran, using different combinations of mitigation techniques. An overview of these simulations is given in table 4.1.

Table 4.1: Overview of different LES cases

	Case 1: Baseline case	**Case 2: Biased case**	**Case 3: Resonator case**	**Case 4: Resonator + Biased case**
A/B Bias	1	0.7	1	0.7
Resonators	Excluded	Excluded	Included	Included

- **Case 1:** This case is considered the baseline case. The goal of this case is to identify the HFD and establish a general understanding about the mode. Therefore, no mitigation technique is applied. The mode is most likely to occur if the fuel is unbiased and no HFD damping resonators are present.
- **Case 2:** Once the HFD is established, the effect of fuel biasing will be analyzed.
- **Case 3:** Next, the effect of only adding high frequency resonators will be analyzed.
- **Case 4:** After seeing the individual influence of the mitigation techniques in case 2 and 3, the effect of adding them both simultaneously will be analyzed.

In this section, the results from the different simulations will be given and discussed. First the frequency response and the spectrograms of the different cases will be evaluated and compared in section 4.1 to see if the mode can be identified. The mode will be visualized in section 4.2. The effect of the fuel biasing, reaction model and resonators will be discussed more in depth in sections 4.4 and 4.5 respectively.

4.1 Mode identification

The modes will be identified through Mause spectrograms. A Mause spectrogram is an overview of the timesignal, the Fourier transformed signal and the spectrogram. Figure 4.1 shows the Mause spectrogram of Case 1. For confidentiality reasons, the pressure signal is shown relative to the operating pressure and the frequency in the FFT is normalized with the frequency of interest. The normalized spectrograms for the other 3 cases can be found in appendix B.1. A summary of the results is given in table 4.2.

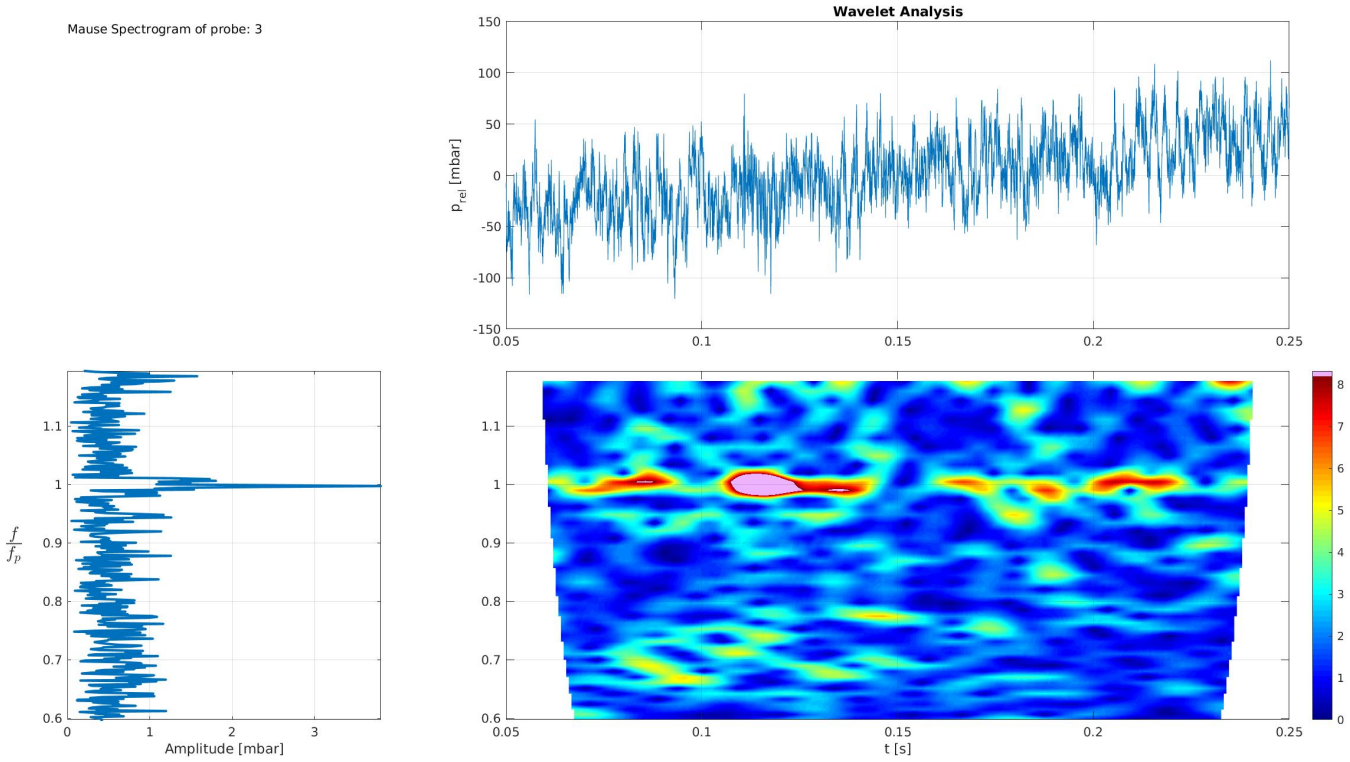

Figure 4.1: Mause Spectogram of Case 1: Baseline case. The pressure signal (top-right) shows p_{rel}, the pressure relative to the operating pressure. The FFT (bottom left) shows the frequencies normalized with the frequency of interest f_p. The spectrogram (bottom right) shows the occurrences of the instabilities during the simulation.

Table 4.2: Summary of HFD events from the Mause Spectrograms of the four LES cases.

	Case 1: Baseline case	**Case 2: Biased case**	**Case 3: Resonator case**	**Case 4: Resonator + Biased case**
Highest amplitude event [s]	0.1 - 0.12	0.12 - 0.14	0.18 - 0.23	0.2 - 0.24
FFT value [mbar]	4	1.5	1.3	1.4
Spectrogram peak value [mbar]	8	4.5	4	4

4.1.1 Spectrograms discussion

Noticeable results from Fig. 4.1 are that the HFD mode is found and has a clear distinct peak compared to the surrounding frequencies. The highest pressure fluctuation amplitudes are around 8 mbar. The instability occurs multiple times within the recorded time range of $t = 0.05$ s to $t = 0.25$ s. A slight pressure drift is seen in the pressure signal as a result of the NRBC. The amplitude of the drift does not indicate large variations in the solution flow field and is therefore deemed insignificant.

When comparing the spectrogram from the LES in figure 4.1 with the spectrograms from the experiments at DLR it becomes clear that the LES under-predicts the magnitude of the pressure fluctuations substantially. In the worst case, the amplitude of the fluctuations in the experiments are 2 to 3 orders of magnitude higher than the amplitudes in the LES case. As discussed in section 2.3.1, the occurrence of a limit cycle oscillation is a balance between the driving and damping factors. On the driving side there is the nonlinear flame response of the system, which is hard to obtain and implement in the flame model [68]. On the damping side, lots of things could be damping the acoustics and thus the FFT results. The large difference in amplitude could additionally mean that the numerical damping from the LES is a non-linear type of damping. A fair amount of simulation settings have been chosen taking economical considerations into account. Increasing mesh fineness, using smaller timesteps with more inner iterations and further tuning of the NRBC could all lead to reducing the numerical damping in the simulations, but it remains questionable to what degree this will help. Further research into this topic would be necessary to draw conclusions about it.

On the other hand, the frequency of the peaks in the FFT of the LES and the experimental results match relatively well and deviate only by 40 Hz. Considering the difficulty of matching the acoustic boundary conditions of the LES with that of the experimental test rig, 40 Hz is deemed reasonably close. This difference could be attributed to some simulation settings, like the adiabatic walls in the simulation. Because no heat loss is taken into account, a slightly different temperature field will be present in the simulations which locally influences the speed of sound and thus also the acoustic boundary conditions.

The mitigation techniques in case 2 and 3 seem to reduce the amplitude of the instabilities. The amplitude of the instability at the frequency of interest is still slightly higher than the surrounding peaks as seen in the Mause Spectrograms in appendix B.1, but they are not as distinct as in the baseline case. Lastly, no additional benefit results from combining the two mitigation techniques since the HFD still occur with the same amplitude and regularity. These results in combination with the discrepancies of the pressure fluctuation amplitudes in the LES and experiments could indicate that the mitigation techniques work relatively well. Since the amplitude of the HFD mode is almost as small as the surrounding peaks, the peaks found in cases 2, 3 and 4 can be interpreted as negligibly small modes.

These findings point towards LES being a quantitative tool indicating whether or not instability will occur and at what frequency, rather than it being a qualitative tool providing accurate instability amplitude predictions.

4.1.2 Coupling of pressure and heat release fluctuations

As discussed in section 2.3.1, thermoacoustic instabilities occur when the heat release fluctuations and pressure fluctuations couple and are within 90° degree phase with each other. Using the center of heat release data explained in section 3.5, useful quantities like the cross-power spectral density, coherence and the phase can be computed to see if and how well the Rayleigh criteria is satisfied.

Figure 4.2 shows the average CPSD and phase of the heat release and pressure fluctuations. The average CPSD of the eight cell cets are computed for the five different axial location from figure 3.7 during the highest amplitude HFD event from case 1. The phase from the second axial row at the frequency of interest is shown for the individual parts of the flame. Figure 4.3 shows the average coherence of the heat release and pressure fluctuations of the same cell sets and during the same HFD event used for the CPSD.

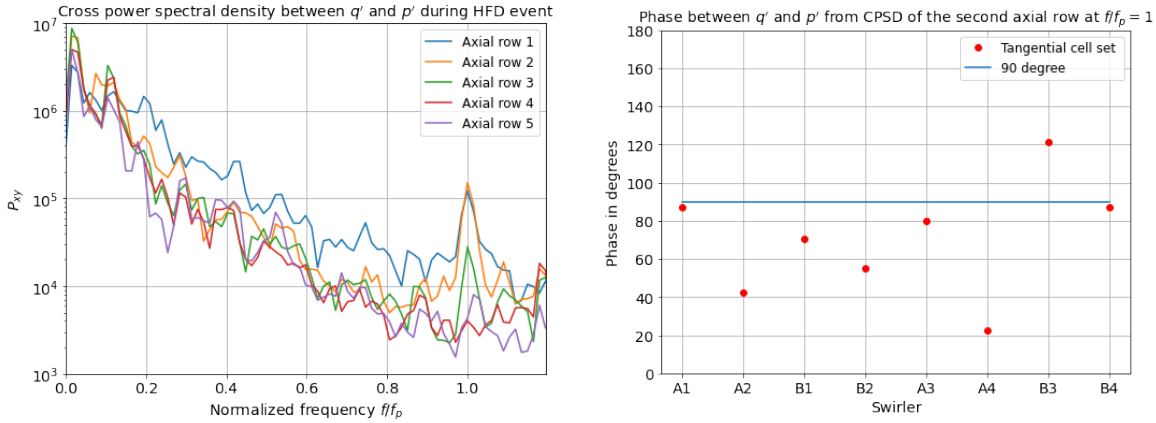

Figure 4.2: Left plot: Cross power spectral density of the pressure and heat release fluctuations during an HFD event, averaged over the eight cell sets at five different axial locations. Frequency is normalized with the frequency of the HFD mode. Right plot: Phase between the heat release and pressure fluctuations extracted from the CPSD for the eight cell sets from the second axial bin.

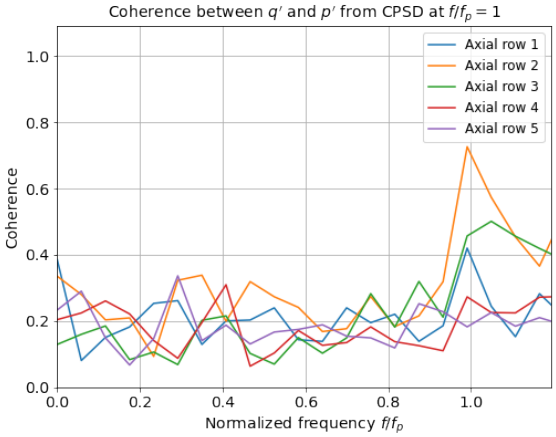

Figure 4.3: Plot showing the coherence of the pressure and heat release fluctuations during an HFD event, averaged over the eight cell sets at five axial locations.

The first thing to note from the CPSD and coherence plots is that there is a distinct peak at the frequency of interest. This peak is especially strong at the first and second axial row. Having a peak at the frequency of interest further confirms the coupling of the acoustics with the flame. The coherence at different frequencies is lower than 0.4 and can be interpreted as random. It then spikes to above 0.7 for the second axial row. This means that not only the power contents of both the pressure and heat release fluctuations are at the frequency of the HFD mode, they are also strongly correlated as can be deducted from the coherence plot. The phase plot shows that the largest part of the heat release fluctuations of the flame are within 90° degree phase with the pressure fluctuations, thus satisfying the Rayleigh criteria. These findings indicate that the HFD found in the simulations is a self excited thermoacoustic instability located near the pilot cone and directly downstream of it.

4.2 Mode shape

In this section, the mode will be visualized. Time signals can be represented as a summation of harmonic functions at different frequencies with different amplitudes and phases. Fast Fourier Transformations basically decompose the signal into these harmonic functions. The pressure field of the cells in the burner and on selected planes has been recorded and Fast Fourier Transformed. Then the complex number containing the amplitude and phase of the mode at the frequency of interest f_p is visualized. This is visible in figure 4.4. A cross-section called the B-plane located between the pilot cone and resonators is shown in figure 4.5. The amplitude of all mode shape figures is given in Pascal.

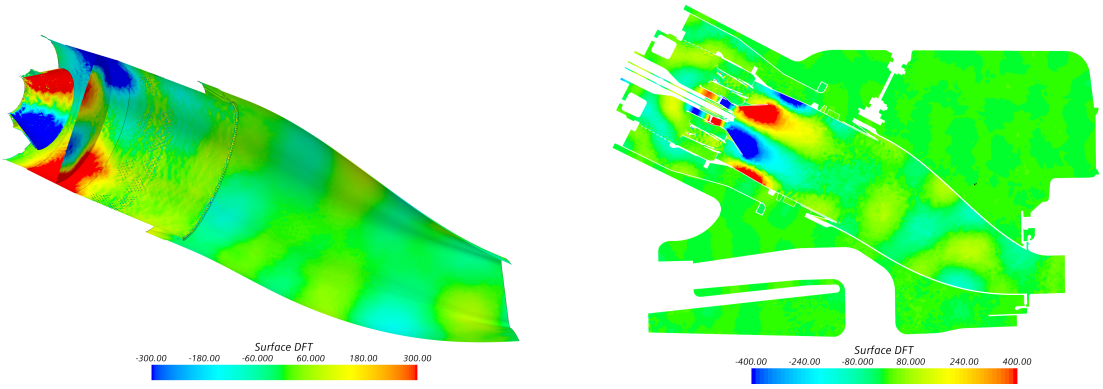

Figure 4.4: Amplitudes of the Fast Fourier Transformed pressure signals at the burner walls and cross sections to visualize the HFD Mode shape in case 1. 3D Burner in left image, midplane cross-section in right image.

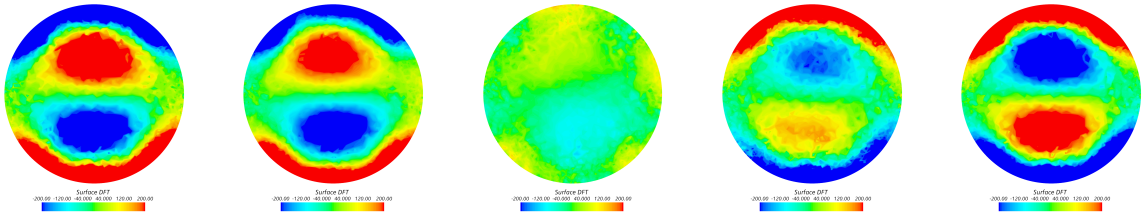

Figure 4.5: Visualization of half a period of HFD mode on plane B in case 1.

The first result of this visualization is the mode shape. Using the nomenclature defined in section 2.2.4, the HFD mode turns out to be a 1T1R mode. The mode is located inside and around the pilot cone. The mode expands upstream into the pilot premixer and downstream into the burner, but is mainly concentrated inside the pilot cone and walls around it. This result is in agreement with the results from the Rayleigh Criteria anlysis done in section 4.1.2. From looking at figure 4.4, it is arguable that the mode also has a 2L component in addition to the 1T1R components, but changing the amplitude scale of the surface FFT narrows down the mode to only the pilot cone and surrounding wall.

As discussed in the previous section, the amplitude of the pressure HFD instability in the baseline case is significantly higher and more distinct than the amplitudes in the other cases. In order to compare the shape of all cases, the scale of the FFT amplitudes is capped at 0.5 mbar and the midplane and B-plane cross-sections are given in figures 4.6 and 4.7.

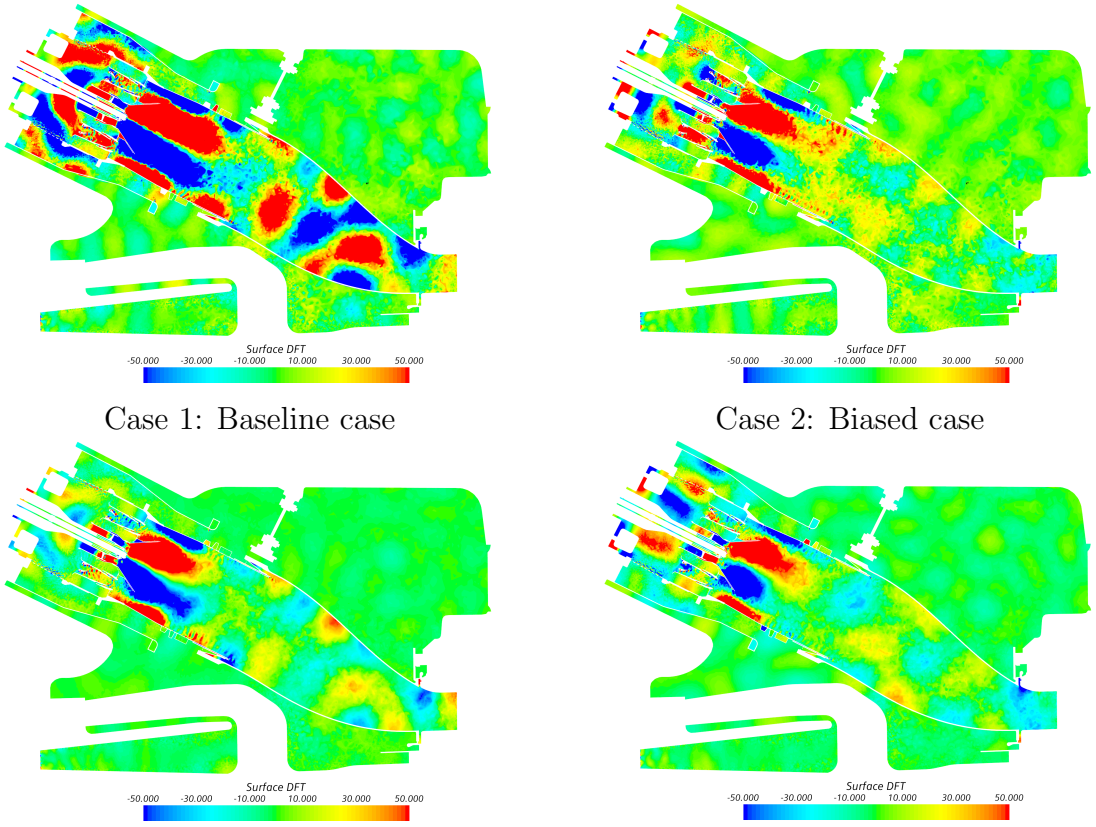

Case 1: Baseline case

Case 2: Biased case

Case 3: Resonator case

Case 4: Resonator + biased case

Figure 4.6: HFD mode shape comparison of the 4 LES cases. Amplitude scale is capped at ± 0.5 mbar to better visualize the modes.

When comparing the midplanes of the four different cases, it becomes clear that the mode is located in the same location every time. Depending on how strong the pressure fluctuations are, it expands further upstream and downstream of the pilot cone. More information about the modes in the different cases can be extracted if the B-plane cross-sections are compared throughout half a period of the instability. The comparison is shown in figure 4.7.

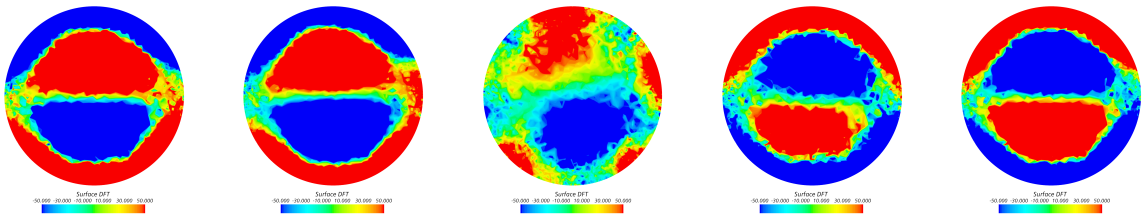

Baseline case (1): Standing mode

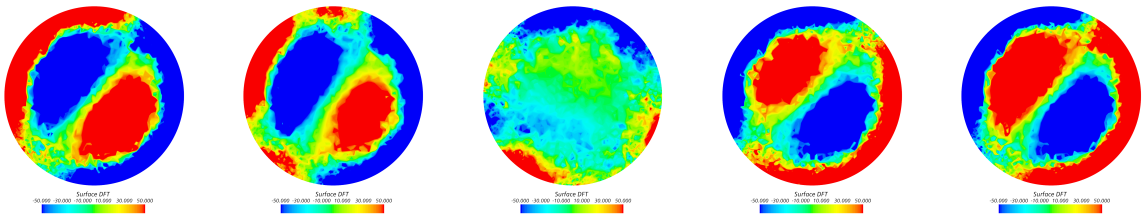

Biased case (2): Standing mode

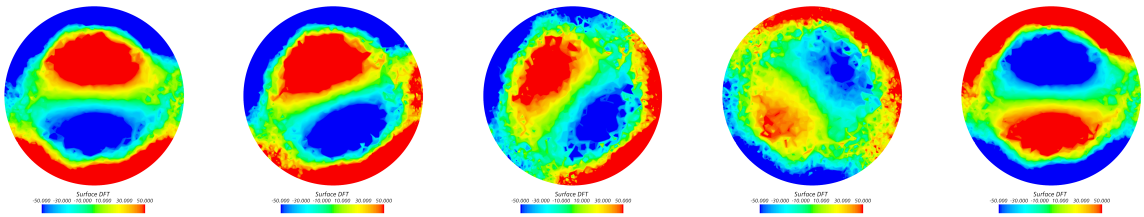

Resonator case (3): Mixed mode

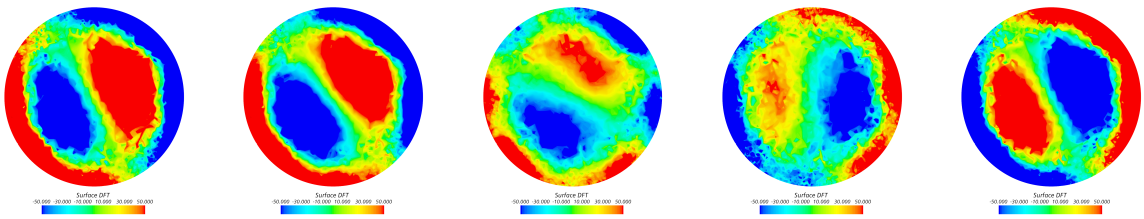

Resonator + biased case (4): Mixed mode

Figure 4.7: Comparison of the mode on the B-plane cross section during half a period for the 4 different LES cases. Amplitude scale is capped at ± 0.5 mbar to better visualize the modes.

The first notable result from figure 4.7 is that all modes have the same 1T1R shape. Differences between them are the orientation of the mode azimuthally and whether the mode is standing or turning. The first two cases show a purely standing mode, which flips after certain time. The other two cases are not purely standing or turning, but seem to a mixed case. The peak amplitudes of the periodic oscillation of the cases are at the same location, but the mode turns in between those peaks. In general, it is difficult to predict whether a standing or a turning/mixed mode will be found in a combustor. They are both observed in practice and understanding why a mode will be standing is still being researched [14].

The second finding is that biasing rotates the location of the peak amplitudes slightly. Case 2 has its pressure anti-nodes downstream of the B swirlers and case 4 has them downstream of the A swirlers. The non-biased cases 1 and 3 have part of the the pressure anti-nodes downstream of an A stage and the other part downstream of a B stage swirler.

Lastly, the LES seems to predict the same mode in every simulation case, even after changing settings which should strongly affect the occurrence of it. The fact that the mode looks the same in every simulation strongly implies that this is the same HFD mode found in the experiments at DLR.

4.3 Potential driving mechanism

Visualizing the modes in the previous section showed some HFD potentially taking place inside the premixing ducts and fuel lines. One of the driving mechanisms of thermoacoustic instabilities is equivalence ratio fluctuations due to the fuel supply as discussed in section 2.4.1. To check whether this could be the cause for HFD in the 8000H combustor, the pressure inside the fuel lines and pilot flame premixer is recorded. The FFT of that data is computed and discussed below.

4.3.1 Fuel line

The pressure data recorded inside the fuel lines showed no clear peak in the FFT except for the pressure signals inside the P- and D-stage fuel lines. These peaks are shown in figure 4.8.

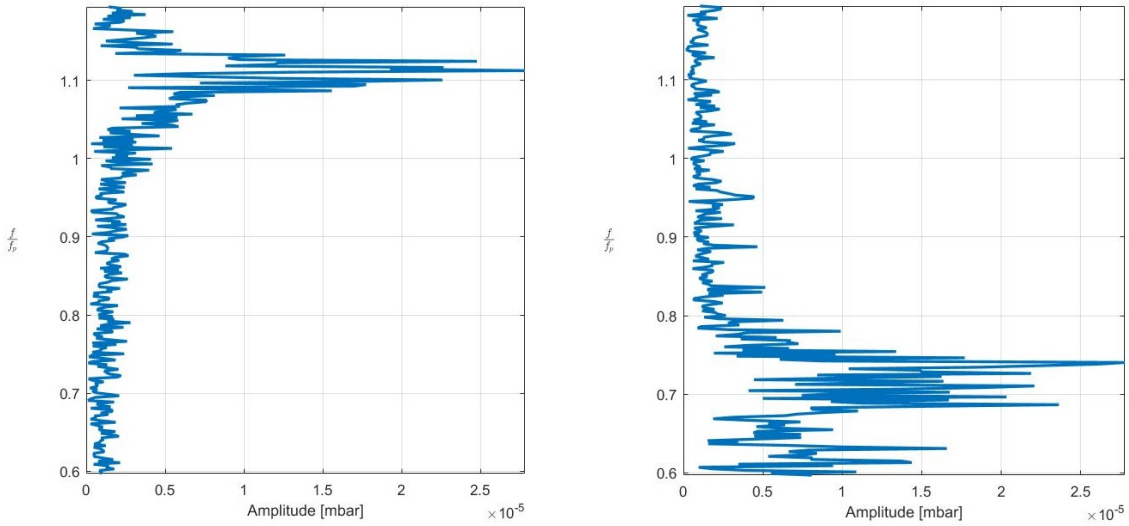

Figure 4.8: FFT of pressure signals for the D-stage (left) and P-stage (right) fuel lines. Frequency normalized with frequency of the HFD mode f_p.

However, these peaks are not at the same frequency of the HFD mode inside the combustor. Contrary to the fuel lines in real combustors, in LES they are designed with an arbitrary short length starting from the inlet boundary condition. This creates the

possibility of having an acoustic mode inside the fuel line similar to that of a duct with two closed ends as seen in figure 2.5. The resonance frequency of the fuel lines in the simulation geometry is calculated using equation (19):

$$f = \frac{nc_0}{2L} \qquad \text{(19 revisited)}$$

Using the speed of sound of the gas in the fuel lines and taking L as the length of the fuel lines in the geometry, the resulting natural frequencies are exactly the same frequencies as the frequencies found from the pressure signals. These peaks are therefore artificially created by the simulation.

Even though it has been pointed out that the amplitude of the oscillations should be interpreted with some care, the amplitude of the pressure fluctuations inside the fuel lines are 10^5 times smaller than the amplitude of the HFD mode and considered negligible. Lastly, the gas has to go through very small fuel injector holes before it mixes with the air. The Mach number in these injector holes can reach values of 0.9. In that case the acoustic fluctuations in the fuel lines should be decoupled from the acoustics inside the combustor. The fuel supply as a driving mechanism for the HFD is therefore excluded as a possible candidate.

4.3.2 Premixer

The same analysis is done for the premixer. The FFT in of the pressure data inside the premixer is given in figure 4.9.

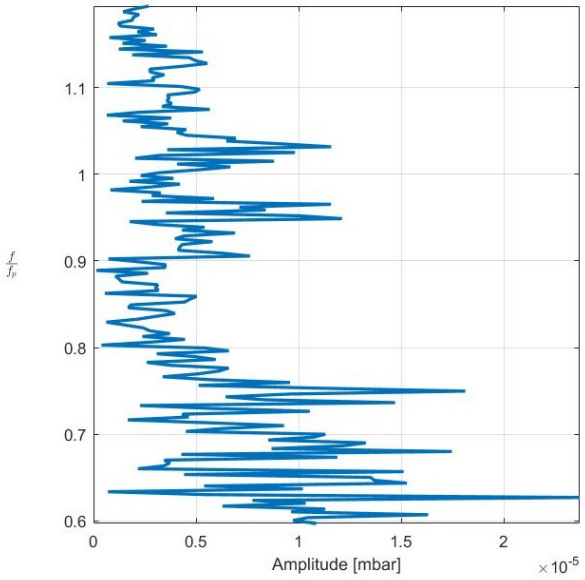

Figure 4.9: FFT of pressure signal in the pilot premixer. Frequency normalized with frequency of the HFD mode f_p.

Again no peak is shown at the frequency of the instability and the overall amplitude of the FFT is multiple orders of magnitude smaller than the amplitude of the HFD.
The convective lengthscale is computed to further argue that this is not the driving mechanism of the HFD. The convective lengthscale of a fluctuation in the premixed normalized with the combustor diameter is calculated in (72):

$$\mathcal{L}_{conv} = \frac{u_0}{f_p D_{can}} = 0.03 \tag{72}$$

where u_0 is the mean flow in the premixer, f_p the peak of interest and D_{can} the combustor diameter. For a velocity fluctuation from the premixer to reach the pilot cone it would have to travel roughly 15 convective lengthscales, at which point the fluctuation will have mostly been dissipated.

4.4 Discussion case 2: effect of fuel biasing and flame model

The amplitude of the HFD in case 2 goes down but does not completely vanish. It is questionable to what extent the HFD can completely vanish in the LES since the amplitudes in the LES are already low compared to the amplitude of HFD events in experiments. Still it is useful to understand the effect of the biasing on the flame and on the HFD.

The effect of the bias can be seen when looking at figure 4.10. This figure shows the time averaged isosurface of the progress variable set at $y = 0.5$ to illustrate how the flame looks. The normalized mean temperature is then projected onto this isosurface to show the effect of the bias. The normalized temperature is defined as $T_{norm} = (T - T_{min})/(T_{max} - T_{min})$.

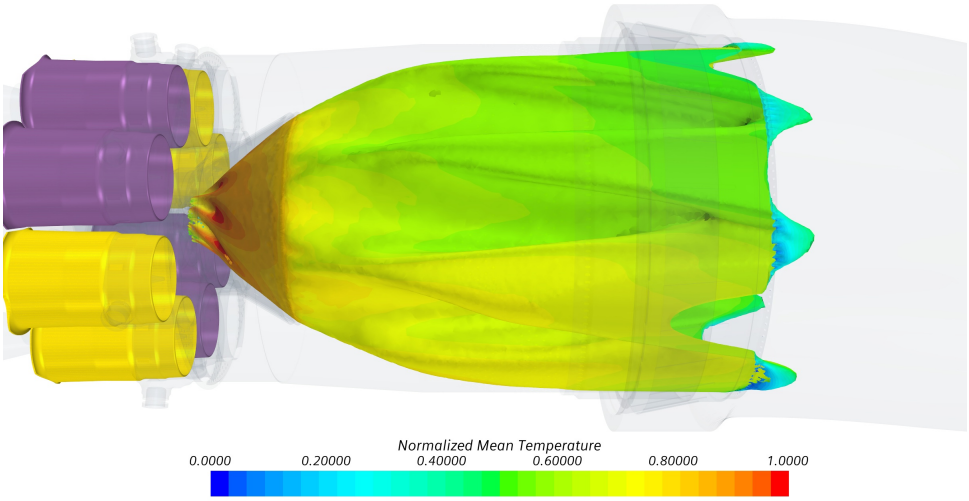

Figure 4.10: Normalized temperature profile projected on the time averaged isosurface of progress variable $y = 0.5$. Temperature is higher in front of the A-stage swirlers (yellow) than in front of the B-stage swirlers (purple).

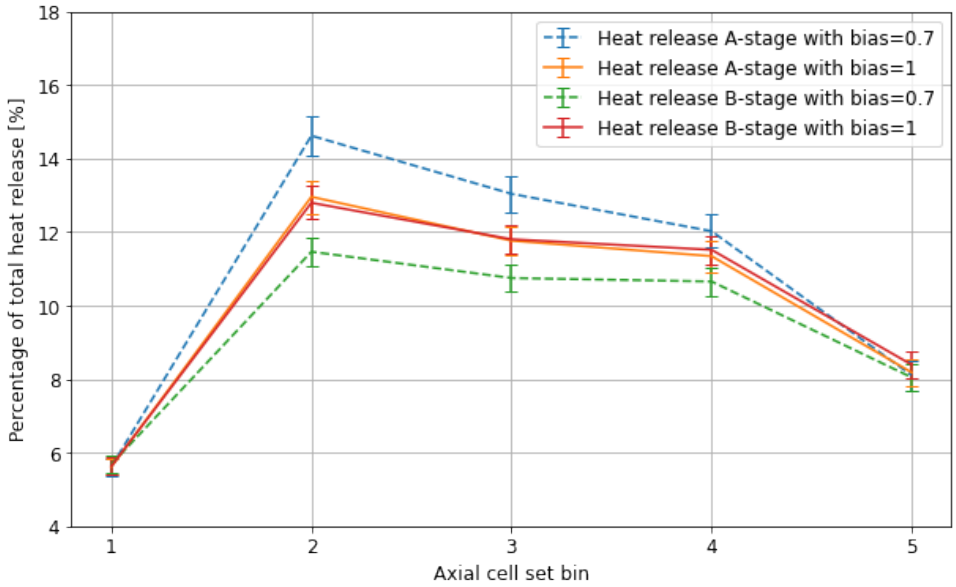

Figure 4.11: Time averaged heat release integral for the A- and B-stage as a percentage of the total heat release of the flame, plotted for the different axial cell set locations. Shown for a flame with a fuel biasing of $\frac{\dot{m}_B}{\dot{m}_A} = 1$ and a flame with a bias of $\frac{\dot{m}_B}{\dot{m}_A} = 0.7$

The a-symmetric temperature profile is clearly visible in figure 4.10. The center of heat release data is used to determine the change in heat release magnitude and location. Figure 4.11 shows this difference in heat release. It is clear that the biasing shifts the heat release from the B to the A stage as expected.

What does not seem to change is the flame length downstream of the A-stages (yellow) and B-stages (purple) respectively. The A-stage receives a larger amount of fuel. This leads to a higher equivalence ratio downstream of the A stage swirlers. A higher equivalence ratio results in a higher flame speed and thus the flame is expected to become shorter downstream of the A-stage swirlers. In a similar way, the flame is expected to become longer downstream of the B-stage swirlers.

The center of heat release data is used to determine the center of heat release for the AB-biased flame. The time-averaged axial center of heat release for all A and B swirler cells is given in figure 4.12. It is clear that the AB-bias works. However, the difference between the axial coordinate of the center of heat release downstream of the A- and B-stage is only in the order of 1 cm, which is small compared to the burner size. Therefore, a more in depth analysis is required to see how the AB-bias affects the flame in the simulation.

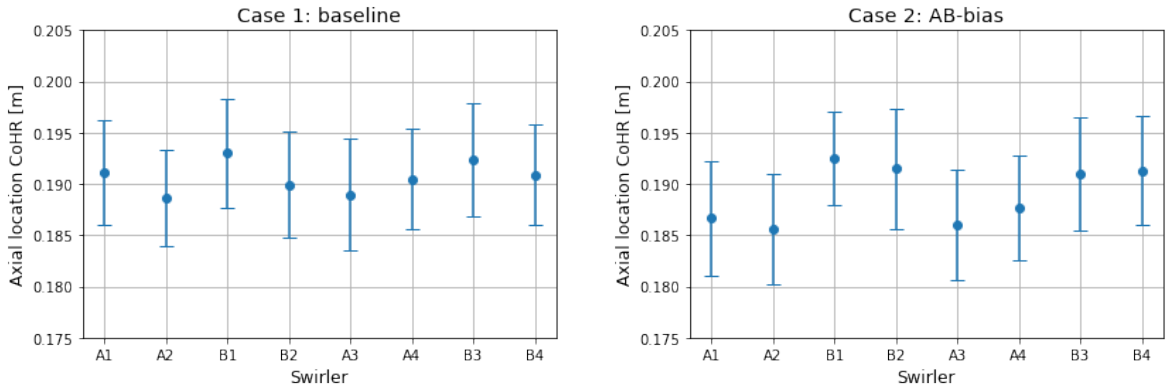

Figure 4.12: Axial center of heat release location for cell sets downstream of the different A- and B-stage swirlers for the baseline case (left) and the AB Bias case (right).

4.4.1 Flame model

In theory, supplying different amounts of fuels to the different fuel stages should lead to differences in equivalence ratios and thus in different flame speeds downstream of the fuel stages. When looking at figure 4.14, it becomes clear that the assumption of different equivalence ratios and thus different flame speeds is correct for the laminar flame speed. Parts of the flame downstream of the A-stage swirlers have a higher laminar flame speed resulting from the higher equivalence ratio there. When looking at figure 4.16 however, it is more difficult to see if the turbulent flame speed also changes as expected. The difference is not as clearly visible as seen in the laminar flame speed. A closer look at the TFC model is therefore necessary.

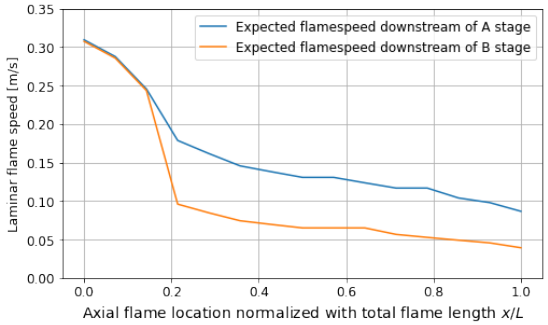

Figure 4.13: Expected laminar flame speed downstream of A- and B-stages using the time averaged equivalence ratio results from the LES at different axial flame locations.

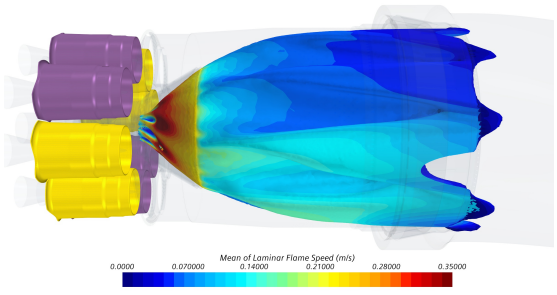

Figure 4.14: Time averaged laminar flame speed projected on the time averaged isosurface of progress variable $y = 0.5$. Laminar flame speed is higher downstream of the A-stage swirlers (yellow) than downstream of the B-stage swirlers (purple).

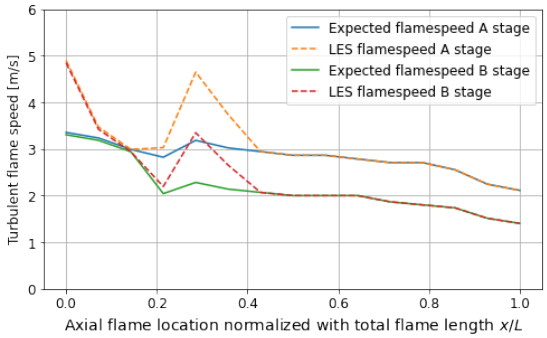

Figure 4.15: Turbulent flame speed from the LES and the expected turbulent flame speed downstream of A- and B-stages using the time averaged equivalence ratio results from the LES at different axial flame locations

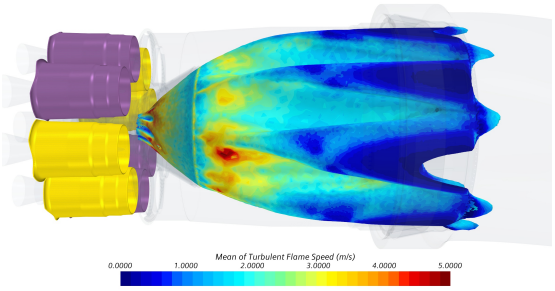

Figure 4.16: Time averaged turbulent flame speed projected on the time averaged isosurface of progress variable $y = 0.5$. Turbulent flame speed is not much higher downstream of the A-stage swirlers (yellow) than downstream of the B-stage swirlers (purple).

Determination of the flame position can roughly be reduced to a balance between diffusion and convection versus the reaction rate as seen in equation (54). Assuming the mesh in the LES is fine enough, the diffusion and convection are well resolved. The bottleneck of accurate flame position calculation then comes down to the reaction term $\dot{\omega}_y$. Therefore the TFC model formulation (55) which is used to calculate the flame movement in space is revisited below. The laminar flame speed is calculated through the Gülder correlation (57). The turbulent flame speed calculation is done through the zimont flame speed correlation (56).

$$\dot{\omega}_y = A\rho_u S_t |\boldsymbol{\nabla} y| \tag{55 revisited}$$

$$S_t = 0.5G\,(u')^{\frac{3}{4}}\, S_l^{\frac{1}{2}} \alpha_u^{-\frac{1}{4}} I_l^{\frac{1}{4}} \tag{56 revisited}$$

$$S_l = ZW\phi^{\eta} e^{-\xi(\phi-1.075)^2} \left(\frac{T_u}{T_0}\right)^{\alpha} \left(\frac{p}{P_0}\right)^{\beta} \tag{57 revisited}$$

Laminar flame speed Starting from the laminar flame speed, the assumption is done that the difference in equivalence ratio should influence the flame speed locally, which is indeed the case. The only cell dependent variables in the equation are the equivalence ratio ϕ, unburnt temperature T_u and pressure p, of which only the equivalence ratio changes significantly. The equivalence ratio is taken from the simulation and the expected laminar flame speed is computed and plotted in figure 4.13. The expected laminar flame speed matches the flame seen in figure 4.14 and the a-symmetry in flame speed is nicely visible, where the laminar flame speed is roughly twice as high for the higher equivalence ratio regions.

Turbulent flame speed In the turbulent flame speed correlation, it is assumed that the integral lengthscale I_l, unburnt thermal diffusivity α_u, stretch factor G and subgrid-scale velocity fluctuations u' barely change for different equivalence ratios. The turbulent flame speed should then scale with $S_t \sim \sqrt{S_l}$. This holds true except for two parts of the flame where the turbulent flame speed turns out to be larger than expected. This is shown in figures 4.15 and 4.16. The expected turbulent flame speed is calculated using the previously derived expected laminar flame speed, α_u and I_l from the simulation and using the general values for the sub-grid scale velocity fluctuations u'. The LES flame speed in figure 4.15 is calculated using the values of u' from the simulation. The LES showed that SGS turbulent kinetic energy has local hotspots where the values go to twice the value of surrounding area. This is the case at the injection into the pilot cone and at the location where the A- and B-stage gas mixture meets the flame, as can be seen in figure 4.16 as the red peaks.

As mentioned in section 3.3.1, the velocity fluctuations u' that go into the model equation are the subgrid-scale modeled fluctuations. This together with the fact that the LES uses an implicit filtering as discussed in 2.6.2 could lead to a problem with the accuracy of the modeled u'. The values of u' will keep changing with the mesh size. Theoretically, when the mesh is so fine that the simulation reaches the DNS limit, the subgrid-scale velocity fluctuations would become zero and the model would then predict zero flame speed [69]. Instead, the burning velocity should reach the laminar flame speed in this limit as the laminar flamelet concept is based on the description of a turbulent flame as a collection of laminar flame elements which are embedded in a turbulent flow [63]. On the other side of the problem is that the u' values will be over-predicted when the cell size is too large. Thus this is a way in which the model can break down.

4.4.2 Multi injector swirl flame

What does not seem to change much due to the equivalence ratio a-symmetry is the flame length. Intuitively speaking, one could guess that the higher equivalence ratio parts of the flame should also become shorter due to the increased turbulent flame speed, and vice versa for the lower equivalence ratio parts. This is not the case as seen in the visualization of the flame in figure 4.10. This section will try to explain why this is not the case for this flame.

The flame in this burner is a complex tulip shaped flame which is more similar to a swirl flame than a jet flame. For lean laminar jet flames, the flame speed and thus the flame height follow a somewhat linear relation with increasing equivalence ratio. When burning under lean conditions, an equivalence ratio increase of $\phi = 0.1$ leads to a change in flame length of roughly 30% as seen in figure 4.17.

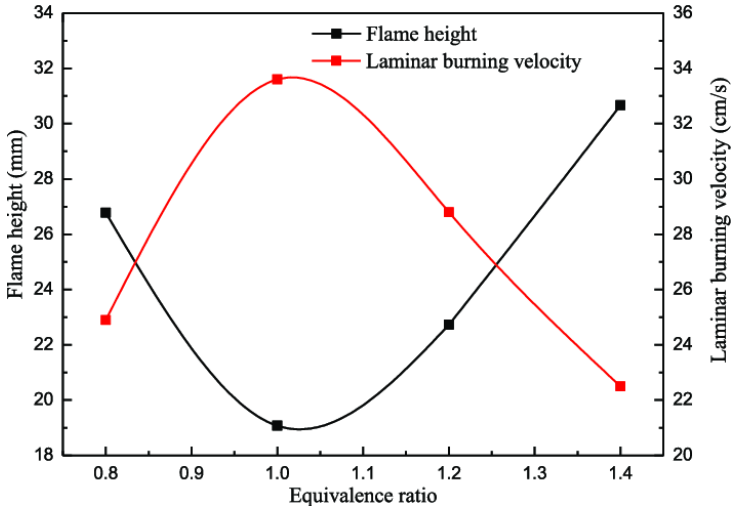

Figure 4.17: Plot of the flame height and laminar burning velocity of a premixed Bunsen flame. Obtained from the work of Wei et al. [70].

The main effects that swirl has on a flame are improved flame stability as a result of recirculation zones and reduced combustion lengths due to better entertainment of ambient fluid and faster mixing [71]. Swirl flames do not vary much in length for different equivalence ratios. An example of this is seen in the experiments of Di Sabatino and Guiberti [72]. They researched the effects of fuel and equivalence ratio on the response of lean premixed swirl flames to acoustic perturbations of the flow. They used flames with different equivalence ratios ranging from $\phi = 0.69$ to $\phi = 0.83$. The length of the flames did not change as much as the intensity at which they burned, as seen in figure 4.18. So even when using a perfectly correct model, it would still be difficult to get a big difference in flame length.

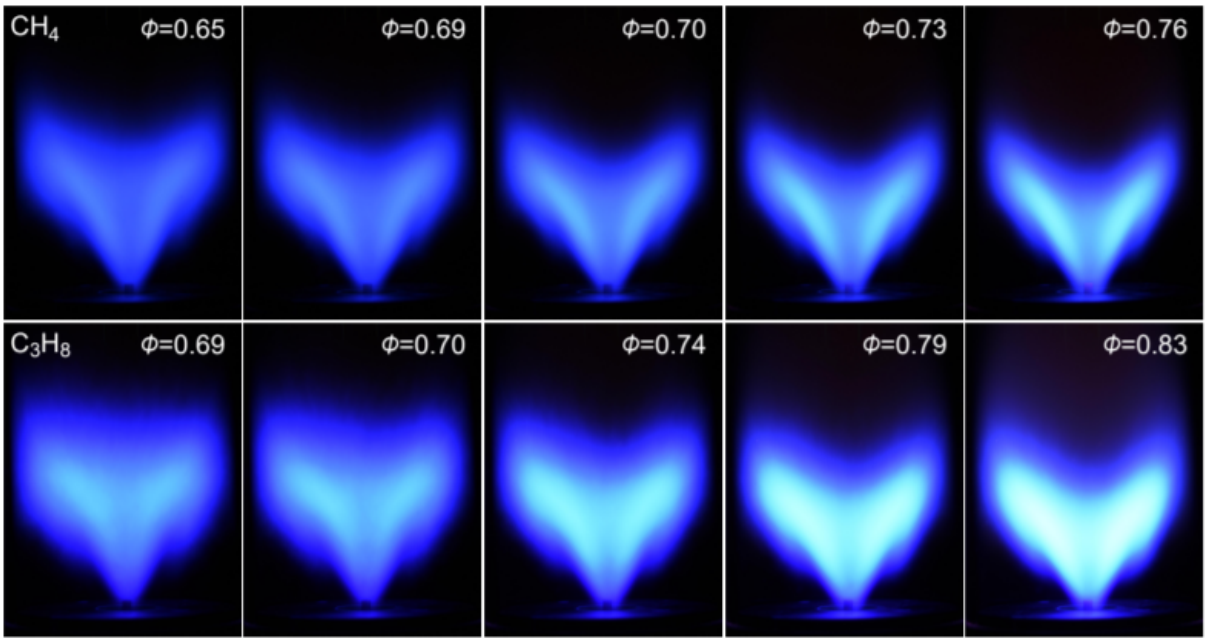

Figure 4.18: Photographs of swirl flame with difference equivalence ratio taken with a digital single-lens reflex camera. Obtained from the work of Di Sabatino and Guiberti [72].

Additionally, the burner has a complex geometry in which different nozzle injectors co-exist and uses the concept of breaking up one monolithic flame into smaller flame elements that anker on the same pilot cone. Advantages of such a configuration are improved volumetric heat release rate, flexible fuel-staging, reduced flame-wall interactions and more control of thermoacoustic instabilities [73]. However, this also leads to more complexity, as the flames are interacting with each other. If a single flame is taken and put in isolation, a reduction in its equivalence ratio should result in a longer flame. But in this burner, parts of the flame are interacting with neighboring flames which could help stabilize the leaner burning flames. This has been shown before by Kwong and Steinberg [74]. They researched the effect of nozzle spacing on lean blow-off in a multinozzle combustor. One of the things they found was that cross-nozzle flame transport due to convection can have a substantial effect on the stability of the flames. The effect this has on the flame in this setup is that the richer burning parts of the flames are preventing the leaner burning parts of the flame from becoming longer.

4.4.3 Conclusion

Taking the previous considerations about the multi injector swirl flame configuration into account, it is assumed that the flame shape is correct. The analysis done on the flame propagation model also indicates that biasing works as expected. The flame gets an a-symmetric temperature profile and does not change much in length. A reason as to why the mode is still found, albeit with a very small amplitude, can be explained by the impact the bias has on the flame and the location of the thermoacoustic instability. From visualizing the mode in section 2.2.4, it has become clear that the HFD is happening inside the pilot cone and directly around it. The fuel biasing however mainly influences the flame further downstream. Only a small fraction of the part of the flame at the HFD location is affected by the bias, as the A/B bias does not affect the part of the flame in the pilot cone.

4.5 Discussion case 3: Effect of resonators

The results of the resonator TF defined in section 3.6 for the HFD damping resonators will be discussed here. Figure 4.19 shows the resulting TF response of the HFD damping resonators. The pressure signals provided to the Welch transformation are taken from $t = 0.05$ s to the final simulation time $t = 0.25$ s.

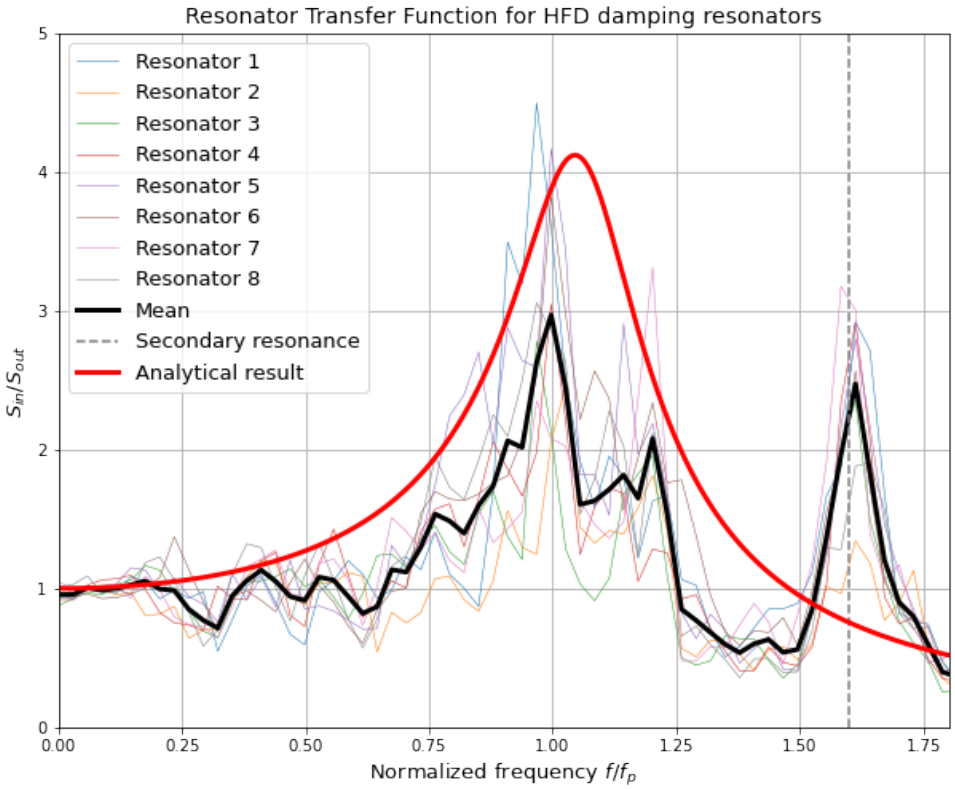

Figure 4.19: Plot of the resonator transfer function for the HFD damping resonators on the 8000H combustor. Black line shows the average response of all 8 resonators. The frequency axis is normalized with the frequency of interest.

Secondary resonance The first thing to note is that there are two peaks, which is unexpected. However, the extra peak turns out to be a secondary peak, resulting from the geometrical resonance frequency of the resonator cavity itself. This is visualized in figure 4.20 A resonant mode similar to that of a duct with two closed ends like in figure 2.5 is present. This is confirmed by computing the natural resonance of the resonator box using equation (19). Using the speed of sound of the gas in the resonator and taking L to be the width of the resonator box, the resulting resonance frequency sits right at the frequency of the second peak, confirming that it is indeed an artificial resonance.

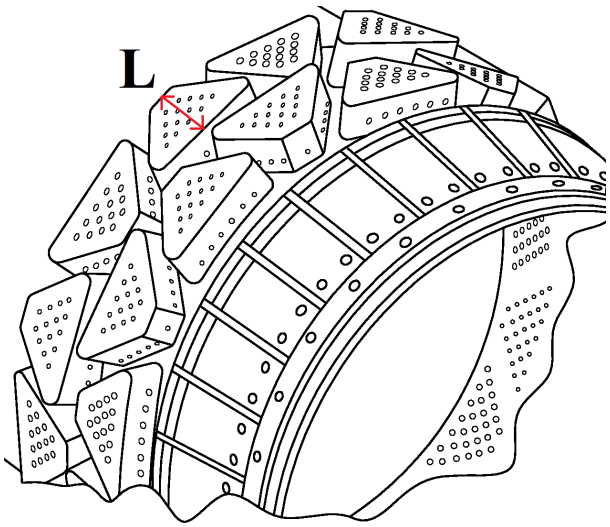

Figure 4.20: Close up of the resonators and their geometry to illustrate the cause of the secondary resonance measured in the LES. **L** shows the length used for the resonance frequency calculation. Figure obtained from Siemens Energy Inc patent [45].

Peak location The next thing to notice is that the first peak of the TF response sits exactly at the frequency of interest. This indicates that the resonant frequency of the resonators are perfectly designed for the frequency of the HFD mode in the burner. In other words, the reactance χ as defined in equation (31) is close to zero and the highest value for the acoustic resistance is achieved at this frequency.

Analytical solution An analytical solution for the resonators transfer function is derived in section 2.5.2 in order to validate the LES results. The analytical pressure ratio equation (44) derived in section 2.5.2 is multiplied with its complex conjugate and the inverse is taken to get a relation for the magnitude ratio of the pressure signals $\frac{\hat{S}_{p2}}{\hat{S}_{p1}} \left(= \frac{\hat{S}_{in}}{\hat{S}_{out}} \right)$. This is equivalent to the resonator transfer function defined in equation (71). This is done for the values V, l S of the resonators used on the 8000H combustor and typical values of c_0 and u_2. The result is shown in figure 4.19 as the red line.

4.5.1 Conclusion

The LES result and the analytical result match reasonably well. The difference in amplitude of the mean LES result and the analytical result can be explained by the spread of the eight individual resonators. The individual resonators show some spread in terms of amplitude. This is likely due to the location of the resonators. They are placed equidistantly around the circumference of the burner. Some resonators will sit on pressure antinodes, thus providing a lot of damping and having higher amplitude peaks in the TF response. Similarly, some resonators will be located at pressure nodes, thus not damping the mode as much as the others. The resonators sitting at pressure nodes are not seeing much pressure fluctuations, and are therefore not showing a large response. The resonators located at pressure anti-nodes show good agreement with the analytical solution and the resonators are therefore assumed to work as expected.

The TF results are strong indications that the HFD damping resonators perform nicely. Two possible reasons remain as to why HFD is still seen in the resonator case. The amplitude of the HFD in the LES is smaller in comparison with experiments. So it could be that this low amplitude residual HFD is negligible. The other explanation is the location of resonators. As discussed in section 2.5.2, the resonators should be placed at the axial location of highest pressure amplitude. From the results of section 4.2 it has become clear that the HFD mode sits in and around the pilot cone. The midplane cross-section in figure 4.4 shows the highest pressure amplitude slightly upstream of the current resonator location. A higher degree of damping is expected if the resonators are thus moved closer to the pilot cone.

5 Conclusions and recommendations

This work was focused on capturing a high frequency thermoacoustic instability occurring in a specific burner design by means of Large Eddy Simulations. The goal was to get more insight about the mode in order to successfully mitigate or even eliminate the mode entirely. To this end, four different cases have been simulated and compared. The results are summarized and recommendations for future work are given in this chapter.

5.1 Conclusions

The baseline case was set up in such a way that it is most susceptible to the thermoacoustic instability. The simulation was successful and the instability was found. The high frequency dynamics found in experiments at DLR showed high amplitude oscillations at a distinct frequency. LES showed instabilities within 40 Hz of that frequency, which is reasonably close to the experimental value. On the other hand, the amplitude of the oscillations was significantly smaller. It is not entirely clear why this is the case, but it is speculated that it is due to simulations settings and simplifications made in order to keep the computational cost relatively low. To further confirm that the pressure oscillations found in the simulations are indeed thermoacoustic oscillations, the coupling between the pressure and heat release oscillations is analyzed. The cross power spectral density and coherence between the heat release and pressure oscillations are computed at different locations of the flame and large correlations were found at the same locations that the mode visualization analysis pointed to. Furthermore, the phase between the pressure and heat release oscillations was within 90° at the location of highest coherence. The Rayleigh criteria is thus satisfied. Lastly, four cases with different operating parameters were simulated. Every simulation showed the occurrence of the mode at the same frequency with the same mode shape. All these findings are strong indications that the mode found in the simulations is the same as the mode found in experiments.

Next, the mode was visualized. Using Fast Fourier Transformation on pressure data at the surface of the combustor and at different planes made it possible to visualize the mode. The mode turned out the be located inside and around the pilot cone of the burner. The mode has a 1T1R shape, i.e. has a transverse and radial component. Depending on how strong the instability occurs, it expands further downstream and upstream of the pilot cone.

Visualizing the mode suggested that the fuel supply to the pilot cone could have been a possible driving mechanism. However, the FFT showed that the frequency peak of the fuel lines were at a different frequency range than that of the thermoacoustic instability, thus not being able to drive the instability in the burner.

After identifying the mode, its sensitivity to simulation settings and operational parameters was analyzed. First a correct flame speed scaling parameter, the TFC rate coefficient A, had to be found. This parameter influences the flame length. On the one hand no unburnt fuel had to go to the turbine section, and on the other hand no flashback should occur. Increasing the TFC rate coefficient from the initial value of $A = 1.5$ to $A = 2.25$ made the flame shorter and increased the amplitude of the HFD. This resulted from more energy being released at the location of the mode, in turn resulting in stronger coupling of the heat release and pressure oscillation. The second change is the fuel biasing. After changing the amount of fuel supplied to the different fuel stages around the flame, an a-symmetric flame temperature profile is obtained. This flame successfully reduced the amplitude of the instability to the same level as the noise amplitudes. The flame length does not change much, which is believed to result from the flame being made up of multiple swirl flames interacting with each other. Lastly, the influence of the Helmhotlz resonators is tested. To this end, a transfer function has been defined relating the power content of the pressure inside and outside the resonators. The resonance frequency of the Helmholtz resonators is exactly at the frequency of the thermoacoustic instability, providing maximum damping. The transfer function results are compared with an analytical solution to test the validity of the LES results and good agreement was found.

Concluding the study, the Rayleigh criteria is satisfied and the mode can be identified using Large Eddy Simulations. Shortening the flame results in a stronger instability. The driving mechanism is still unclear, but mitigation techniques like biasing the fuel and adding Helmholtz resonators successfully dampens the instability.

5.2 Recommendations

As stated before, the amplitude of the instabilities is severely underestimated in the LES. It is believed that this is largely due to numerical damping, resulting from simulation settings choices keeping the calculation computationally cheap. Now that the mode is identified, a more in depth analysis can be done by increasing this computational cost. This can be achieved by increasing the amount of inner iterations, reducing the timestep and refining the mesh around the geometrical location of the thermoacoustic instability. Furthermore, a different progress variable closure model than the Turbulent Flame Speed closure model can be used. This model was selected in order to change the flame length so that the instability would be more easily found. This however adds a new uncertainty to the calculation, as the real flame length is now unknown. Using a closure model without a tuning parameter like the Kinetic Rate closure model will get rid of this uncertainty.

Recommendations on the application of the mitigation technique can also be made. First the fuel biasing technique. Fuel biasing is done to reduce symmetry of the flame and in turn also the coupling of the resonant mode with the flame. However, one of the findings of this research is that the resonant mode is located inside the pilot cone. The fuel biasing on the other hand mainly affects the flame directly downstream of the pilot cone. The oscillation amplitude reduction is therefore less effective. It is recommended to change the fuel distribution to the pilot flame instead, in order to affect the mode more strongly. This is of course limited due to flame stability considerations, and more research is needed to know to what extent this will influence the instability. Next, recommendations for the resonators can be made. Overall the resonators work as expected. A way to further improve their damping effect is to place them more upstream from their current location, as this will move them closer to the source of the thermoacoustic instability and damp it even more. Also this needs to be further explored as this will change the cooling airflow requirements and therefore result in different operating conditions.

Appendices

A Appendix - Chapter 3

A.1 TFC A coefficient study

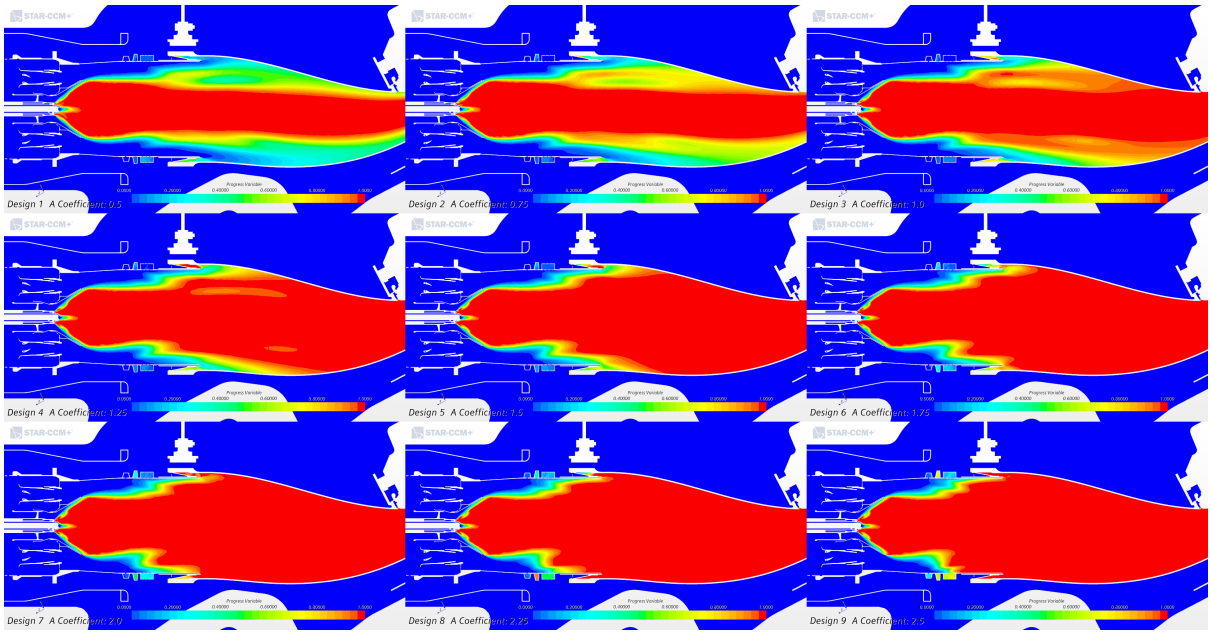

Figure A.1: Design study showing the Progress Variable for the RANS simulation at different TFC rate coefficients A, ranging from 0.5 to 2.5 in steps of 0.25.

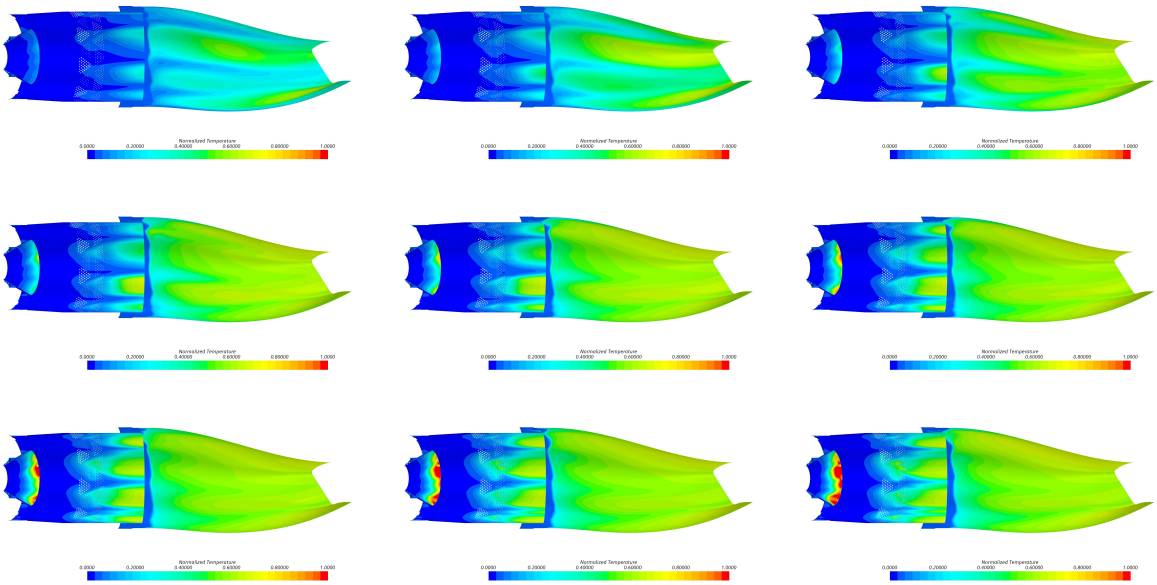

Figure A.2: Design study showing the normalized surface temperature for the RANS simulation at different TFC rate coefficients A, ranging from 0.5 to 2.5 in steps of 0.25.

B Appendix - Chapter 4

B.1 Normalized Spectrograms of DLR Probes in LES

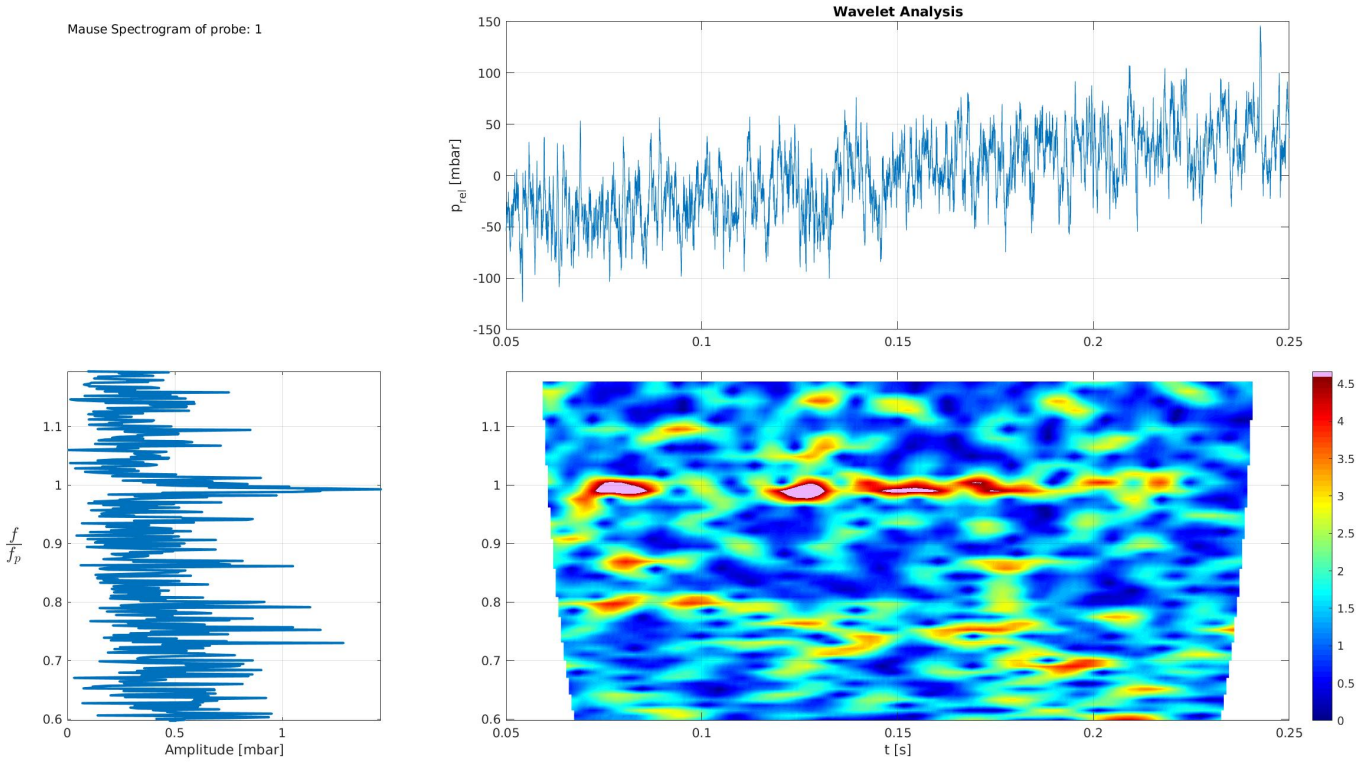

Figure B.1: Spectrogram of Case 2: Biased case. Data of pressure probe A1.

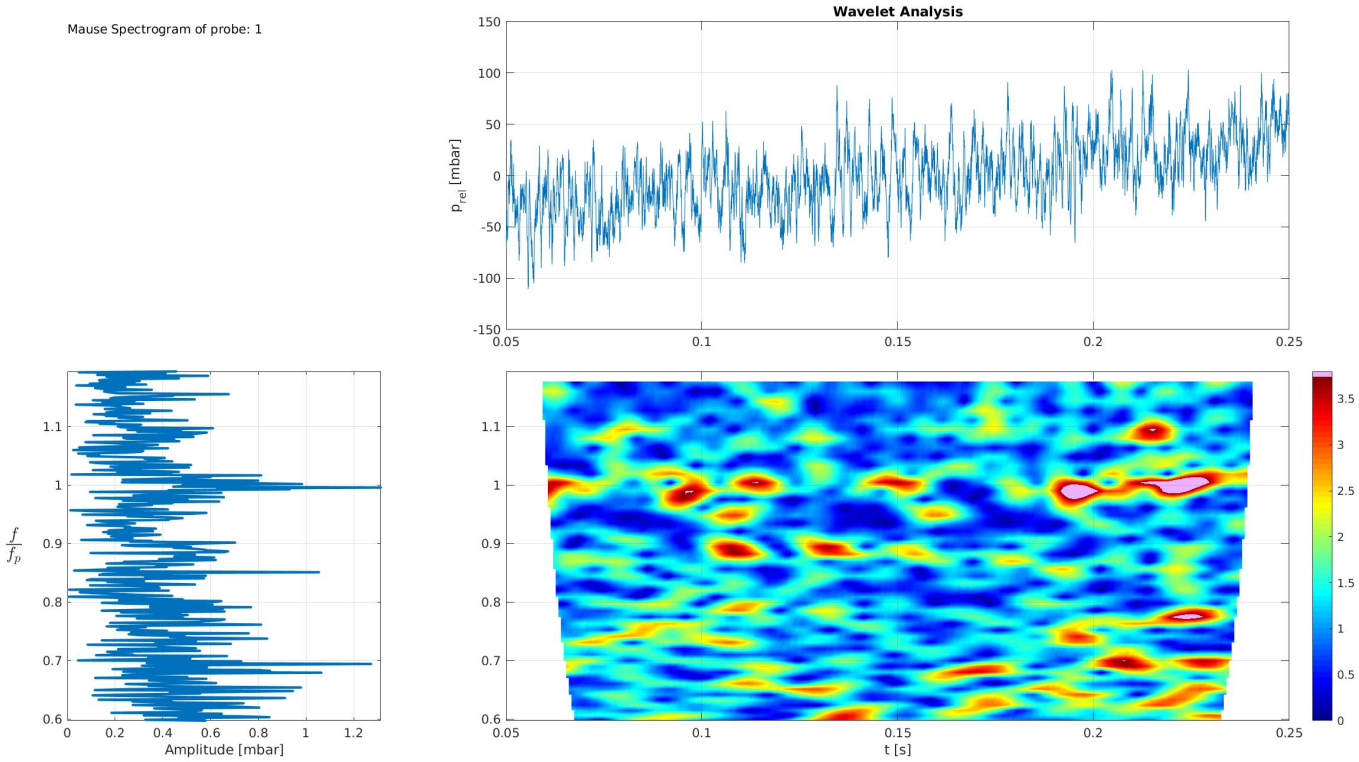

Figure B.2: Spectogram of Case 3: Resonator case. Data of pressure probe A1.

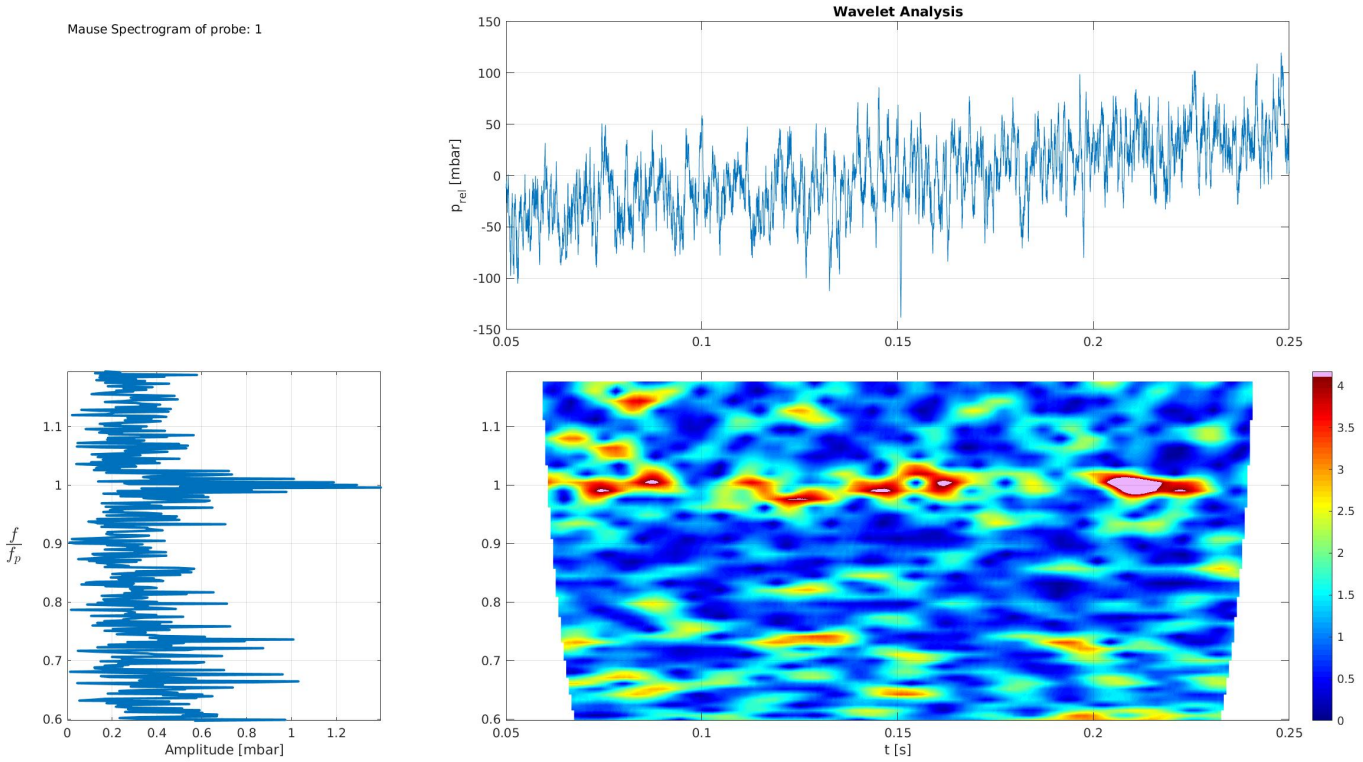

Figure B.3: Spectrogram of Case 4: Resonator + Biased case. Data of pressure probe A1.

B.2 AB-bias study

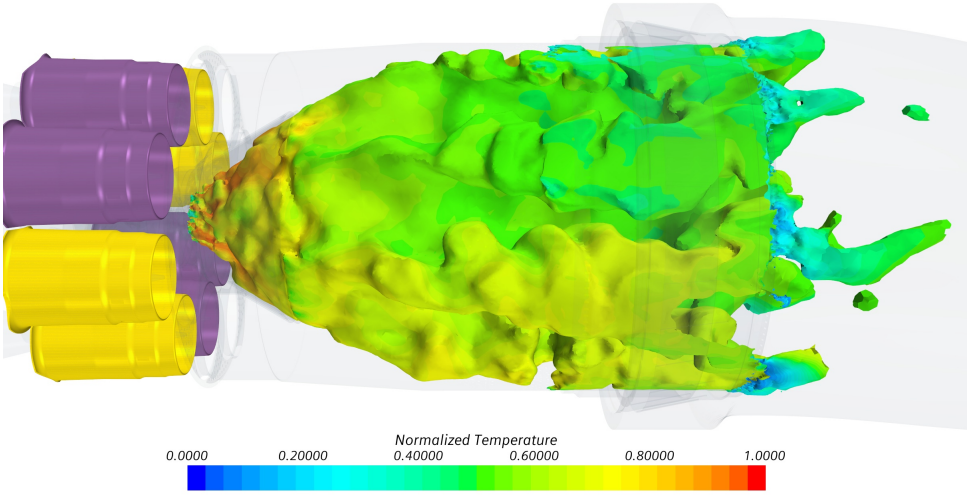

Figure B.4: Normalized temperature profile projected on the instantaneous isosurface of progress variable $y = 0.5$. Temperature is higher in front of the A-stage swirlers (yellow) than in front of the B-stage swirlers (purple).

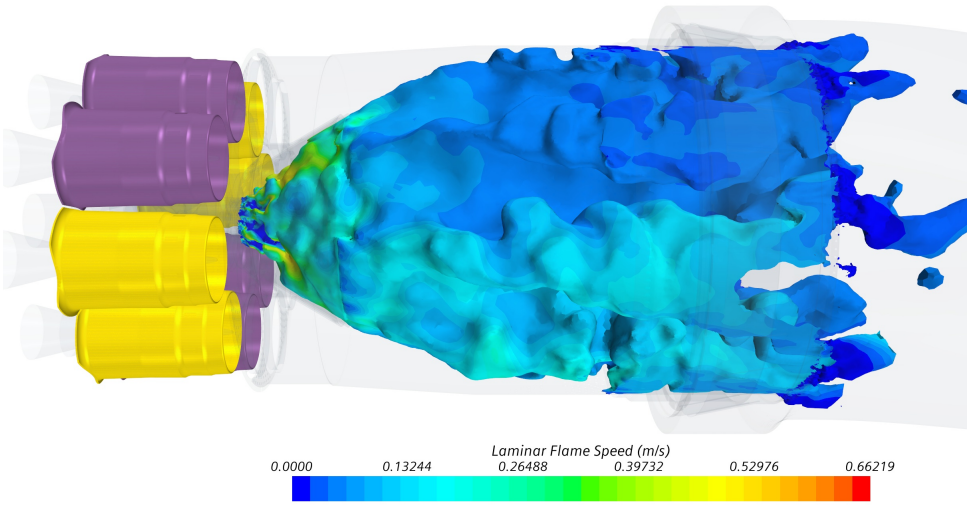

Figure B.5: Laminar flame speed projected on the instantaneous isosurface of progress variable $y = 0.5$. Laminar flame speed is higher in front of the A-stage swirlers (yellow) than in front of the B-stage swirlers (purple).

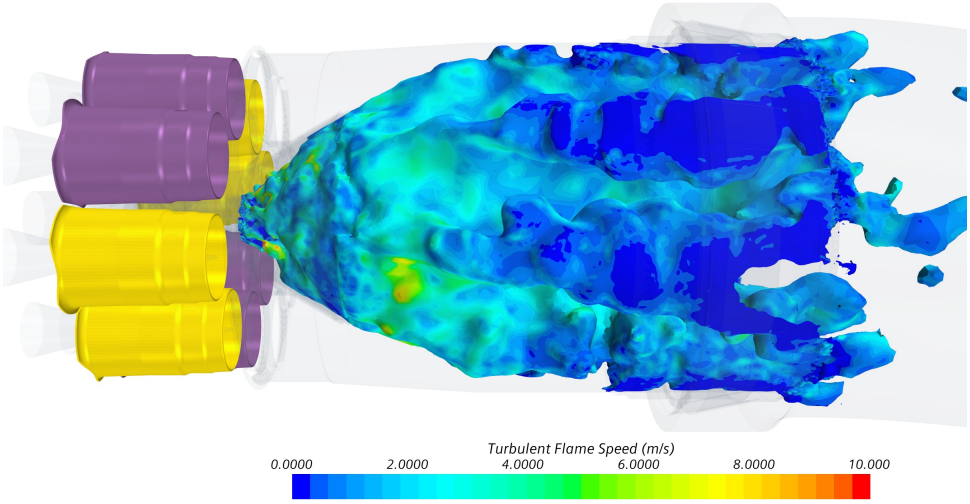

Figure B.6: Turbulent flame speed projected on the instantaneous isosurface of progress variable $y = 0.5$.

Bibliography

[1] Y. Huang and V. Yang, "Dynamics and stability of lean-premixed swirl-stabilized combustion," *Progress in energy and combustion science*, vol. 35, no. 4, pp. 293–364, 2009.

[2] J. O'Connor and T. Lieuwen, "Further characterization of the disturbance field in a transversely excited swirl-stabilized flame," *Journal of Engineering for Gas Turbines and Power*, vol. 134, no. 1, 2012.

[3] I. Hernández, G. Staffelbach, T. Poinsot, J. C. R. Casado, and J. B. Kok, "Les and acoustic analysis of thermo-acoustic instabilities in a partially premixed model combustor," *Comptes rendus mécanique*, vol. 341, no. 1-2, pp. 121–130, 2013.

[4] T. C. Lieuwen and V. Yang, *Combustion instabilities in gas turbine engines: operational experience, fundamental mechanisms, and modeling*. American Institute of Aeronautics and Astronautics, 2005.

[5] F. Culick and V. Yang, "Prediction of the stability of unsteady motions in solid-propellant rocket motors," 1992.

[6] Siemens-Energy, *Sgt6-8000h heavy-duty gas turbine*, [Online; accessed February 17, 2021], 18-02-2019. [Online]. Available: `https://press.siemens.com/global/en/pressrelease/siemens-h-class-gas-turbines-achieve-one-million-operating-hours`.

[7] F. T. Nieuwstadt, J. Westerweel, and B. J. Boersma, *Turbulence: introduction to theory and applications of turbulent flows*. Springer, 2016.

[8] P. K. Kundu, I. M. Cohen, D. R. Dowling, and T. Grétar, *Fluid mechanics*. Elsevier/AP, 2016.

[9] N. Peters, *Turbulent combustion*, 2001.

[10] J. Warnatz, U. Maas, R. W. Dibble, and J. Warnatz, *Combustion*. Springer, 2006.

[11] D. E. Winterbone and A. Turan, *Chapter 15 - Combustion and Flames*, Second Edition. Butterworth-Heinemann, 2015, pp. 323–344, ISBN: 978-0-444-63373-6. DOI: `https://doi.org/10.1016/B978-0-444-63373-6.00015-0`.

[12] P. Palies, "Stabilization and dynamic of premixed swirling flames: Prevaporized, stratified, partially, and fully premixed regimes," 2020.

[13] S. W. Rienstra and A. Hirschberg, "An introduction to acoustics," *Eindhoven University of Technology*, vol. 18, p. 19, 2004.

[14] T. Poinsot and D. Veynante, *Theoretical and numerical combustion*. RT Edwards, Inc., 2005.

[15] M. Norton and S. Drew, *VIBRATION GENERATED SOUND — Fundamentals*, S. Braun, Ed. Oxford: Elsevier, 2001, pp. 1443–1455, ISBN: 978-0-12-227085-7. DOI: `https://doi.org/10.1006/rwvb.2001.0207`. [Online]. Available: `https://www.sciencedirect.com/science/article/pii/B0122270851002071`.

[16] L. E. Kinsler, A. R. Frey, A. B. Coppens, and J. V. Sanders, *Fundamentals of acoustics*. John wiley & sons, 1999.

[17] T. Dammers, "Numerical study on the driving and damping of high-frequency instabilities in a jet flame combustor," 2020.

[18] C. Lahiri, "Acoustic performance of bias flow liners in gas turbine combustors," 2014.

[19] S. Evesque, W. Polifke, and C. Pankiewitz, "Spinning and azimuthally standing acoustic modes in annular combustors," in *9th AIAA/CEAS Aeroacoustics Conference and Exhibit*, 2003, p. 3182.

[20] W. Polifke, "Six lectures on thermoacoustic combustion instability," in *21st CISM-IUTAM Int. Summer School on Measurement, Analysis and Passive Control of Thermoacoustic Oscillations*, 2015, 87–Seiten.

[21] J. O'Connor, V. Acharya, and T. Lieuwen, "Transverse combustion instabilities: Acoustic, fluid mechanic, and flame processes," *Progress in Energy and Combustion Science*, vol. 49, pp. 1–39, 2015.

[22] S. Ducruix, T. Schuller, D. Durox, and S. Candel, "Combustion dynamics and instabilities: Elementary coupling and driving mechanisms," *Journal of propulsion and power*, vol. 19, no. 5, pp. 722–734, 2003.

[23] J. W. S. B. Rayleigh, *The theory of sound*. Macmillan, 1896, vol. 2.

[24] M. C. Janus, G. A. Richards, M. J. Yip, and E. H. Robey, "Effects of ambient conditions and fuel composition on combustion stability," in *Turbo Expo: Power for Land, Sea, and Air*, American Society of Mechanical Engineers, vol. 78699, 1997, V002T06A035.

[25] A. P. Dowling and S. R. Stow, "Acoustic analysis of gas turbine combustors," *Journal of propulsion and power*, vol. 19, no. 5, pp. 751–764, 2003.

[26] I. Hughes and A. Dowling, "The absorption of sound by perforated linings," *Journal of Fluid Mechanics*, vol. 218, pp. 299–335, 1990.

[27] C. J. Goy, S. R. James, S. Rea, T. Lieuwen, and V. Yang, "Monitoring combustion instabilities: E. on uk's experience," *Combustion Instabilities in Gas Turbine Engines: Operational Experience, Fundamental Mechanisms, and Modeling*, vol. 210, pp. 163–175, 2005.

[28] T. Lieuwen and B. T. Zinn, "The role of equivalence ratio oscillations in driving combustion instabilities in low nox gas turbines," in *Symposium (International) on combustion*, Elsevier, vol. 27, 1998, pp. 1809–1816.

[29] J. G. Lee, K. Kim, and D. Santavicca, "Measurement of equivalence ratio fluctuation and its effect on heat release during unstable combustion," *Proceedings of the Combustion Institute*, vol. 28, no. 1, pp. 415–421, 2000.

[30] G. C. Oates, *The aerothermodynamics of aircraft gas turbine engines*. Air Force Aero Propulsion Laboratory, Air Force Wright Aeronautical ..., 1978, vol. 2.

[31] E. Zukoski, "Combustion instability sustained by unsteady vortex combustion," in *21st Joint Propulsion Conference*, 1985, p. 1248.

[32] J. Seume, N. Vortmeyer, W. Krause, J. Hermann, C.-C. Hantschk, P. Zangl, S. Gleis, D. Vortmeyer, and A. Orthmann, "Application of active combustion instability control to a heavy duty gas turbine," in *Turbo Expo: Power for Land, Sea, and Air*, American Society of Mechanical Engineers, vol. 78675, 1997, V001T05A007.

[33] P. Berenbrink and S. Hoffmann, "Suppression of dynamic combustion instabilities by passive and active means," in *ASME Turbo Expo 2000: Power for Land, Sea, and Air*, Citeseer, 2000.

[34] D. Zhao and A. S. Morgans, "Tuned passive control of combustion instabilities using multiple helmholtz resonators," *Journal of sound and vibration*, vol. 320, no. 4-5, pp. 744–757, 2009.

[35] D. T. Harrje and F. H. Reardon, *Liquid propellant rocket combustion instability*. Scientific, Technical Information Office, National Aeronautics, and Space ..., 1972, vol. 1, p. 413.

[36] F. Langfeldt, H. Hoppen, and W. Gleine, "Resonance frequencies and sound absorption of helmholtz resonators with multiple necks," *Applied Acoustics*, vol. 145, pp. 314–319, 2019.

[37] A. Selamet, H. Kim, and N. T. Huff, "Leakage effect in helmholtz resonators," *The Journal of the Acoustical Society of America*, vol. 126, no. 3, pp. 1142–1150, 2009.

[38] D. Gysling, G. Copeland, D. McCormick, and W. Proscia, "Combustion system damping augmentation with helmholtz resonators," *J. Eng. Gas Turbines Power*, vol. 122, no. 2, pp. 269–274, 2000.

[39] C. Bourquard and N. Noiray, "Stabilization of acoustic modes using helmholtz and quarter-wave resonators tuned at exceptional points," *Journal of Sound and Vibration*, vol. 445, pp. 288–307, 2019.

[40] J. B. Sewell and P. A. Sobieski, "Monitoring of combustion instabilities: Calpine's experience," *Combustion Instabilities in Gas Turbine Engines: Operational Experience, Fundamental Mechanisms, and Modeling*, vol. 210, pp. 147–162, 2005.

[41] B. Eisenhower, G. Hagen, A. Banaszuk, and I. Mezić, "Passive control of limit cycle oscillations in a thermoacoustic system using asymmetry," *Journal of applied mechanics*, vol. 75, no. 1, 2008.

[42] N. Noiray, M. Bothien, and B. Schuermans, "Investigation of azimuthal staging concepts in annular gas turbines," *Combustion Theory and Modelling*, vol. 15, no. 5, pp. 585–606, 2011.

[43] J. Cohen, G. Hagen, A. Banaszuk, S. Becz, and P. Mehta, "Attenuation of gas turbine combustor pressure oscillations using symmetry breaking," in *49th AIAA Aerospace Sciences Meeting including the New Horizons Forum and Aerospace Exposition*, 2011, p. 60.

[44] D. James, "A solution for noise associated with a series staged dle combustion system," in *International Pipeline Conference*, vol. 36207, 2002, pp. 1231–1234.

[45] J. E. P. Bilbao, S. M. Martin, and D. M. Ritland, "Air biasing system in a gas turbine combustor," 10,054,313, 2018. [Online]. Available: `https://patents.google.com/patent/US10054313B2/en?oq=US10054313B2`.

[46] D. Laera, G. Campa, S. M. Camporeale, E. Bertolotto, S. Rizzo, F. Bonzani, A. Ferrante, and A. Saponaro, "Modelling of thermoacoustic combustion instabilities phenomena: Application to an experimental test rig," *Energy Procedia*, vol. 45, pp. 1392–1401, 2014.

[47] W. Jones and B. E. Launder, "The prediction of laminarization with a two-equation model of turbulence," *International journal of heat and mass transfer*, vol. 15, no. 2, pp. 301–314, 1972.

[48] D. C. Wilcox, "Formulation of the kw turbulence model revisited," *AIAA journal*, vol. 46, no. 11, pp. 2823–2838, 2008.

[49] S. B. Pope, *Turbulent flows*, 2001.

[50] P. Sagaut, *Large eddy simulation for incompressible flows: an introduction*. Springer Science & Business Media, 2006.

[51] P. Lampitella, "Large eddy simulation for complex industrial flows," 2014.

[52] Fumiya, *Large eddy simulation (les)*, [Online; accessed February 15, 2021], 2016. [Online]. Available: `https://caefn.com/openfoam/les`.

[53] J. Smagorinsky, "General circulation experiments with the primitive equations: I. the basic experiment," *Monthly weather review*, vol. 91, no. 3, pp. 99–164, 1963.

[54] E. R. Van Driest, "On turbulent flow near a wall," *Journal of the aeronautical sciences*, vol. 23, no. 11, pp. 1007–1011, 1956.

[55] F. Nicoud and F. Ducros, "Subgrid-scale stress modelling based on the square of the velocity gradient tensor," *Flow, turbulence and Combustion*, vol. 62, no. 3, pp. 183–200, 1999.

[56] Siemens PLM Software, *Star-ccm+ theory guide*, 2019.

[57] J. Van Oijen, F. Lammers, and L. De Goey, "Modeling of complex premixed burner systems by using flamelet-generated manifolds," *Combustion and Flame*, vol. 127, no. 3, pp. 2124–2134, 2001.

[58] V. Zimont, W. Polifke, M. Bettelini, and W. Weisenstein, "An efficient computational model for premixed turbulent combustion at high reynolds numbers based on a turbulent flame speed closure," 1998.

[59] Ö. L. Gülder, "Turbulent premixed flame propagation models for different combustion regimes," in *Symposium (International) on Combustion*, Elsevier, vol. 23, 1991, pp. 743–750.

[60] U. Gruschka, B. Janus, J. Meisl, M. Huth, and S. Wasif, "Uln system for the new sgt5-8000h gas turbine: Design and high pressure rig test results," in *Turbo Expo: Power for Land, Sea, and Air*, vol. 43130, 2008, pp. 913–919.

[61] H. Krediet, "Prediction of limit cycle pressure oscillations in gas turbine combustion systems using the flame describing function," *University of Twente, Enschede*, 2012.

[62] T. Indlekofer, "Evaluation of starccm+ to predict thermoacoustic instabilities using large eddy simulation," 2017.

[63] T. Echekki and E. Mastorakos, *Turbulent combustion modeling: Advances, new trends and perspectives*. Springer Science & Business Media, 2010, vol. 95.

[64] V. Zimont and V. Battaglia, "Rans, les and hybrid rans/les turbulent premixed combustion tfc model," in *Joint meeting of the Scandinavia–Nordic and Italian sections of the combustion institute*, 2003, pp. 18–21.

[65] G. Boudier, L. Gicquel, T. Poinsot, D. Bissieres, and C. Bérat, "Comparison of les, rans and experiments in an aeronautical gas turbine combustion chamber," *Proceedings of the Combustion Institute*, vol. 31, no. 2, pp. 3075–3082, 2007.

[66] S. M. Kay, *Fundamentals of statistical signal processing*. Prentice Hall PTR, 1993.

[67] P. Stoica, R. L. Moses, *et al.*, "Spectral analysis of signals," 2005.

[68] S. Tachibana, K. Saito, T. Yamamoto, M. Makida, T. Kitano, and R. Kurose, "Experimental and numerical investigation of thermo-acoustic instability in a liquid-fuel aero-engine combustor at elevated pressure: Validity of large-eddy simulation of spray combustion," *Combustion and Flame*, vol. 162, no. 6, pp. 2621–2637, 2015.

[69] A. Lipatnikov and J. Chomiak, "Turbulent flame speed and thickness: Phenomenology, evaluation, and application in multi-dimensional simulations," *Progress in energy and combustion science*, vol. 28, no. 1, pp. 1–74, 2002.

[70] Z. Wei, H. Zhen, C. W. Leung, C. S. Cheung, and Z. Huang, "Heat transfer characteristics and the optimized heating distance of laminar premixed biogas-hydrogen bunsen flame impinging on a flat surface," *International journal of hydrogen energy*, vol. 40, no. 45, pp. 15 723–15 731, 2015.

[71] N. Syred and J. Beer, "Combustion in swirling flows: A review," *Combustion and flame*, vol. 23, no. 2, pp. 143–201, 1974.

[72] F. Di Sabatino, T. F. Guiberti, J. P. Moeck, W. L. Roberts, and D. A. Lacoste, "Fuel and equivalence ratio effects on transfer functions of premixed swirl flames," *Journal of Propulsion and Power*, vol. 36, no. 2, pp. 271–284, 2020.

[73] S. Jella, W. Kwong, A. Steinberg, J. Park, T. Lu, J. Bergthorson, and G. Bourque, "Attached and lifted flame stabilization in a linear array of swirl injectors," *Proceedings of the Combustion Institute*, 2020.

[74] W. Y. Kwong and A. M. Steinberg, "Effect of internozzle spacing on lean blow-off of a linear multinozzle combustor," *Journal of Propulsion and Power*, vol. 36, no. 4, pp. 540–550, 2020.